

12 High-Velocity Clouds

Bart P. Wakker¹ · Hugo van Woerden²

¹Supported by NASA and NSF; affiliated with Department of Astronomy, University of Wisconsin, Madison, WI, USA

²Kapteyn Astronomical Institute, Rijksuniversiteit Groningen, Groningen, The Netherlands

1	<i>Introduction</i>	589
2	<i>Sky Maps: Clouds and Complexes</i>	591
2.1	The Deviation Velocity	591
2.2	Mapping the HVCs	592
2.3	Features of the HVC Sky	595
2.4	Sky Coverage	595
2.5	HVC Kinematics	597
2.6	Ionized HVCs	599
3	<i>The Determination of Cloud Distances and Metallicities</i>	600
3.1	HVC Distances from Indirect Methods	600
3.1.1	H α Intensity	600
3.1.2	Pressure Equilibrium	601
3.1.3	Velocity Gradients	601
3.1.4	The Virial Theorem	601
3.2	Absorption-Line Method for Determining Distances	602
3.2.1	Suitable Stellar Candidates Projected onto the HVC	603
3.2.2	Spectra and Photometry to Characterize the Candidates	603
3.2.3	High-resolution Spectra of Stars at Distances Bracketing that of the HVC	603
3.3	Considerations for Metallicity Measurements	604
3.3.1	HI Small-Scale Structure	605
3.3.2	Depletion onto Dust	605
3.3.3	Presence of Ionized Hydrogen	605
3.3.4	Elemental Ionization Fractions	605
3.4	Strength of the Absorption Lines	606
3.5	Measured Distances and Metallicities	609
4	<i>Physical Properties of the HVCs</i>	610
4.1	Small-Scale Structure	610
4.2	Timescales	613
4.2.1	The Time it Will Take for a Cloud to Reach the Galactic Plane	613
4.2.2	The Time for the Cores to Shift Substantially Relative to Each Other	613
4.2.3	The Time a Core takes to Move Across its Own Width	614
4.2.4	The Time for a Core to Double its Size	614

4.3	Ionization Structure and Volume Density	614
4.4	Molecules and Dust	615
5	<i>Hot Gas Associated with HVCs</i>	617
6	<i>HVCs in and Around Other Galaxies</i>	622
6.1	A Face-on Galaxy: M 101	622
6.2	An Edge-on Galaxy: NGC 891	623
6.3	A High-Inclination Galaxy: NGC 2403	623
6.4	A Low-Inclination Galaxy: NGC 6946	624
6.5	The Nearest Spiral Galaxies: Messier 31 and 33	625
6.6	High-Velocity and Extraplanar Gas in Other Galaxies	626
6.7	Accretion of Gas by Galaxies	627
7	<i>Origins of the High-Velocity Clouds</i>	627
7.1	The Galactic Fountain	628
7.2	Tidal Streams	630
7.3	Low-Metallicity Accretion	631
7.3.1	Fragmentation in a Hot Halo	632
7.3.2	Cold, Filamentary Streams	633
7.3.3	Sweeping up of Coronal Gas by Fountain Flows	634
7.4	Summary of Origins	634
	<i>References</i>	636

Abstract: The high-velocity clouds (HVCs) are gaseous objects that do not partake in differential galactic rotation, but instead have anomalous velocities. They trace energetic processes on the interface between the interstellar material in the Galactic disk and intergalactic space. Three different processes appear to be responsible for the formation of HVCs. First, supernovae in the Galactic disk create hot gas that vents into the halo, cools and rains back down, in a process generically termed the “Galactic Fountain,” in which gas circulates between the disk and halo at a rate of a few $M_{\odot} \text{ yr}^{-1}$. This implies that the interstellar medium (ISM) circulates through the halo on timescales of a Gyr. Second, gas streams are formed by tides working on nearby dwarf galaxies (with a possible contribution from ram pressure); this applies specifically to the Magellanic Stream, which was extracted from the Small Magellanic Cloud. Third, low-metallicity clouds are accreting onto the Milky Way, at a present-day rate of about $0.4 M_{\odot} \text{ yr}^{-1}$. Such infall causes the Milky Way to grow and continue forming stars. The source of the infalling material may lie in the cooling of hot ($T > 10^6$ K) intergalactic gas that permeates space, or in cold ($T < 10^5$ K) accretion streams that are theoretically predicted to transport material from intergalactic filaments to galaxies. This chapter describes the observed locations, velocities, and physical conditions of the HVCs. Also included is a discussion of the methods used to derive their distances and metallicities, as well as of the resulting values. Finally, the different origins of the HVCs are discussed.

1 Introduction

Spiral galaxies have a number of different constituents. Dark matter is responsible for most of the gravity well, stars emit light, and everything is permeated by the interstellar medium (ISM), from which stars form. In turn, the structure of the ISM is determined by the feedback of matter and energy from the stars, as well as by the infall of new material.

Most of the dense ISM is concentrated in the Galactic plane, and rotates around the Galactic Center, just as the stars do. However, several energetic processes lead to gas moving at anomalous velocities, and this gas plays a role in our understanding of the evolution of the Galaxy. These processes include the “Galactic Fountain,” caused by supernovae that heat the ISM and lift it up a few kpc, into the lower halo, where it cools and rains back down (Shapiro and Field 1976; Bregman 1980; Kahn 1981; de Avillez and Breitschwerdt 2005). This circulation redistributes heavy elements and energy; the rate of circulation is likely to be dependent on the supernova rate, while the radial extent of the mixing will depend on the precise balance between various factors, such as the supernova rate, the gravitational potential, and the thermal evolution of the gas. A second process that generates gas at anomalous velocities is the infall of low-metallicity gas, which provides new fuel for star formation. Such gas can be provided by interactions with passing galaxies (i.e., as tidal streams – see e.g., Gardiner and Noguchi 1996; Mastroiello et al. 2005; Connors et al. 2006; Besla et al. 2007), or by instabilities in the massive, large (>200 kpc), hot (10^6 K) coronae of ionized gas that surround the galaxies (Maller and Bullock 2004; Stocke et al. 2006; Wakker and Savage 2009). Alternatively, cold ($T < 10^5$ K) gas may stream into galaxies along intergalactic filaments (Kereš and Hernquist 2009), or it may be swept along by Galactic Fountain clouds (Fraternali and Binney 2008; Marasco et al. 2011). Such newly accreted gas is needed in models of the chemical evolution of the Galaxy, which require star formation to be fed by continuing accretion, at a present-day inflow rate of $\sim 0.4 M_{\odot} \text{ yr}^{-1}$ of material with a metallicity $Z \sim 0.1$ times solar (Chiappini 2008).

Observationally, the gas moving at anomalous velocities is seen in the form of the “high-velocity clouds” (HVCs). Over time, this term has undergone a gradual change in meaning. A detailed summary of the historical development of the study of the HVCs was presented by van Woerden et al. (2004) in Chapter 1 of their monograph on the high-velocity clouds. Originally, the term HVC was applied to interstellar absorption lines at velocities $>20 \text{ km s}^{-1}$ relative to the Sun, which were seen in the spectra of high-latitude stars (Adams 1949; Münch 1952; Schlüter et al. 1953). Later, it was mostly applied to high-latitude neutral hydrogen clouds seen in 21-cm emission with velocities relative to the Local Standard of Rest (LSR) $>80 \text{ km s}^{-1}$ (Muller et al. 1963; Oort 1966). HI clouds at velocities $|v_{\text{LSR}}| = 40\text{--}80 \text{ km s}^{-1}$ were called “intermediate-velocity clouds” (IVCs). Throughout the 1970s and 1980s, 90 and 100 km s^{-1} were also (inconsistently) considered as velocity limits. Wakker (1991) adapted the definition by proposing to use the “deviation velocity” (v_{DEV}), the difference between the observed velocity of the gas and the maximum velocity that can be understood in a simple model of differential galactic rotation. In this definition HVCs have $|v_{\text{DEV}}| > 90 \text{ km s}^{-1}$ and IVCs have $|v_{\text{DEV}}| = 30\text{--}90 \text{ km s}^{-1}$. This has been the working definition since. However, it has not always been strictly adhered to, as the current HVC and IVC catalogues are still based on the old definitions.

Following their discovery, research on HVCs went into three main directions. First, the mapping of the HVC sky, which culminated in the surveys of Giovanelli (1980), Bajaja et al. (1985), and Hulsbosch and Wakker (1988), and in the whole-sky HVC catalogue and definition of HVC complexes (groups of clouds with similar location and velocity) by Wakker and van Woerden (1991). Second, detailed mapping and characterizing of the physical properties of individual clouds (Giovanelli et al. 1973; Davies et al. 1976; Giovanelli and Haynes 1977; Schwarz and Oort 1981; Wakker and Schwarz 1991). Third, attempts at finding an explanation for their origin, with Oort (1966, 1970) presenting the first comprehensive list. His discussion is still generally valid, although the details were much expanded and refined over the following 40 years. Major refinements include the idea of the Galactic Fountain (put forward by Shapiro and Field 1976 and applied to HVCs by Bregman 1980), the understanding of the Magellanic Stream as a tidal feature (proposed by Fujimoto and Sofue 1976 and Lin and Lynden-Bell 1982), and the arguments that HVCs are distant, possibly even Local Group objects (Blitz et al. 1999; Braun and Burton 1999).

Starting in the 1980s, but taking off in the late 1990s, developments in instrumentation and the availability of space observatories and large ground-based telescopes led to the detection of absorption associated with HVCs in the spectra of distant halo stars and UV-bright extragalactic objects (i.e., QSOs and Seyfert galaxies). These studies yielded measurements of HVC distances and metallicities (e.g., Kuntz and Danly 1996; Lu et al. 1998; van Woerden et al. 1999a; Wakker et al. 1999, 2007, 2008; Richter et al. 2001b). When UV absorption-line studies of tracers of hot gas (O VI, C IV) in directions away from the 21-cm HVCs also started showing high-velocity gas (Sembach et al. 1995, 2003; Fox et al. 2004, 2006; Lehner and Howk 2011) the term HVC was extended beyond just the HI clouds. In addition, deep 21-cm observations of other galaxies have revealed HI gas moving at anomalous velocities (van der Hulst and Sancisi 1988; Braun and Thilker 2004; Fraternali et al. 2004, Oosterloo et al. 2007), and by analogy the HVC name was also applied to such objects.

This chapter will use an expansive definition of the term “HVC,” taking it to include the “classical” 21-cm HVCs and IVCs, as well as the high-velocity gas seen in UV absorption lines and the extragalactic anomalous-velocity clouds. ➤ Section 2 presents the observational definition for the Galactic HVCs and discusses the objects that are seen in the sky. ➤ Section 3 summarizes the methods used to determine the distances and metallicities of the clouds, with

our current knowledge of these quantities given in [Sect. 3.5](#). Using these results, [Sect. 4](#) summarizes the physical properties of the clouds. The UV absorption line studies of the hot component of the high-velocity cloud phenomenon are discussed in [Sect. 5](#). Extragalactic HVCs are summarized in [Sect. 6](#). Finally, in [Sect. 7](#) the different explanations that have been put forward for the origin of the HVCs are evaluated.

2 Sky Maps: Clouds and Complexes

2.1 The Deviation Velocity

To best capture the idea that the HVCs represent gas that does not take part in galactic rotation, a basic observational definition was proposed by Wakker (1991). He defined the “deviation velocity,” v_{DEV} , which is the difference between the observed velocity and the maximum velocity that can easily be understood in terms of differential galactic rotation. For a particular direction it is found by calculating

$$\begin{aligned} v_{\text{DEV}} &= v_{\text{LSR}} - v_{g,\text{min}} \text{ if } v_{\text{LSR}} < 0 \\ v_{\text{DEV}} &= v_{\text{LSR}} - v_{g,\text{max}} \text{ if } v_{\text{LSR}} > 0. \end{aligned}$$

Here v_{LSR} is the observed velocity relative to the Local Standard of Rest (LSR) and $v_{g,\text{min,max}}$ are the minimum and maximum possible velocities for rotating disk gas in this direction, $v_g(l, b, d)$. The latter can be found using geometrical relations giving the galactocentric radius (R) and height above the plane (z) as function of distance in the line of sight (d) for a given longitude (l) and latitude (b), combined with a prescription for $v(R)$, the rotation velocity as function of galactocentric radius (i.e., the Galactic rotation curve). It also requires a value for R_0 , the distance of the Sun to the Galactic Center, which is about 7.9 kpc (see [Chap. 16](#) by Feast in this volume).

$$\begin{aligned} v_g(l, b, d) &= \left(\frac{R_0}{R} v(R) - v(R_0) \right) \sin l \cos b \\ R(l, b, d) &= R_0 \sqrt{\cos^2 b \left(\frac{d}{R_0} \right)^2 - 2 \cos b \cos l \left(\frac{d}{R_0} \right) + 1} \\ z(l, b, d) &= d \sin b. \end{aligned}$$

For this chapter, the Galactic rotation curve is assumed to be flat with velocity $v(R) = 220 \text{ km s}^{-1}$ at radii $R > 0.5 \text{ kpc}$, and solid-body closer to the center. Then these three relations can be used to calculate v_{LSR} for all distances between 0 and d_{max} , with d_{max} defined as the distance where the sightline leaves the disk. Many different prescriptions are possible for the edge of the disk. The one that is used in this chapter assumes that the disk has a radius of 26 kpc and thickness $z_1 = 2 \text{ kpc}$ for $R < R_0$, flaring parabolically to $z_2 = 6 \text{ kpc}$ at $R = 3R_0$, so that:

$$\begin{aligned} R_{\text{max}} &= 26 \text{ kpc} \\ z_{\text{max}} &= z_1 \text{ if } R < R_0 \\ z_{\text{max}} &= z_1 + (z_2 - z_1) \times \frac{(R/R_0 - 1)^2}{4} \text{ if } R > R_0. \end{aligned}$$

2.2 Mapping the HVCs

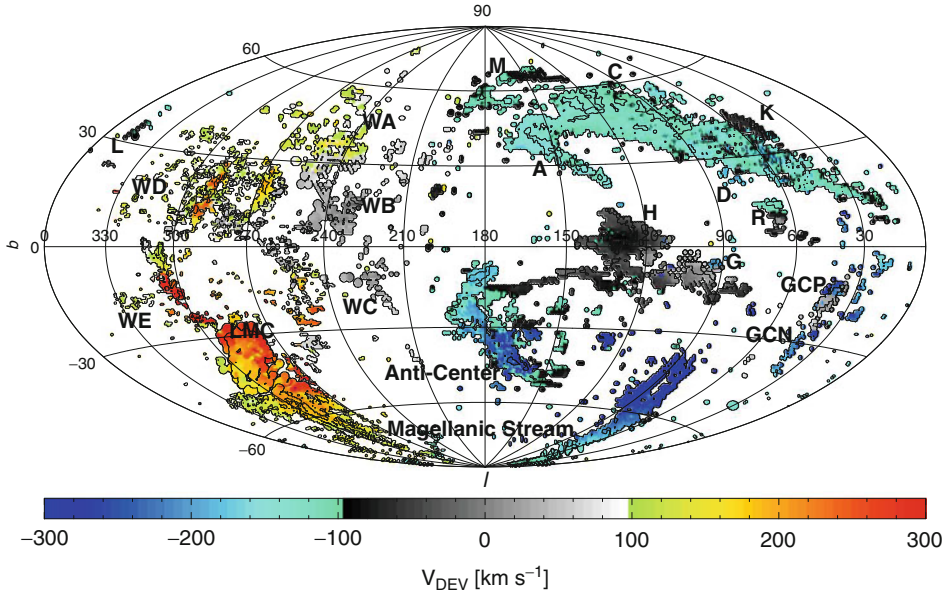
The history of the mapping of the HVCs was reviewed by Wakker and van Woerden (1997) and Wakker (2004). Most of the early observations covered only part of the sky or had rough sampling relative to the size of the telescope beam. The first all-sky survey of high-velocity gas with $|\nu_{\text{LSR}}| > 90 \text{ km s}^{-1}$ was provided by the combination of the lists of Hulsbosch and Wakker (1988) and Bajaja et al. (1985). The former was made using the Dwingeloo telescope and covered the northern sky (declinations $> -23^\circ$) on a $1^\circ \times 1^\circ$ grid, with a 0.5° beam, 16 km s^{-1} velocity resolution, and $5\text{-}\sigma$ detection limit 0.05 K , while the latter (with the Argentinian Villa Elisa telescope) covered declinations $< -18^\circ$ on a $2^\circ \times 2^\circ$ grid, with detection limit 0.08 K . Both datasets were published as a list of HVC profile components, giving longitude, latitude, LSR velocity, and peak brightness temperature. Information about line widths and shapes was mostly lost, but for a typical line width of 20 km s^{-1} , the 5σ detection limits correspond to column densities of ~ 2.0 and $3.0 \times 10^{18} \text{ cm}^{-2}$, respectively. Wakker and van Woerden (1991) used these two datasets to construct the first (and so-far only) all-sky catalogue of the HVCs.

A more complete survey of the HI sky, the “Leiden-Argentina-Bonn” or LAB survey was constructed by Kalberla et al. (2005). This survey combined the northern (declination $> -30^\circ$) “Leiden-Dwingeloo Survey” of Hartmann and Burton (1997) with a complementary survey of the southern sky, again made using the Villa Elisa telescope (Arnal et al. 2000). Both surveys cover the sky on a $0.5^\circ \times 0.5^\circ$ grid, with 1.03 km s^{-1} velocity channels, an rms noise of 0.07 K , and are fully (internally consistently) corrected for stray-radiation effects. Morras et al. (2000) used the southern survey to construct a much improved list of southern HVC components. Wakker et al. (2011) discovered that the published LAB spectra still require a small correction, in the sense that an underlying broad gaussian ($\nu = -22 \text{ km s}^{-1}$, $T_B = 0.0473 \text{ K}$, $\text{FWHM} = 167 \text{ km s}^{-1}$, corresponding to $N(\text{HI}) = 1.5 \times 10^{19} \text{ cm}^{-2}$) needs to be removed. This component is most likely either a residual baseline fitting error, or a small error in the stray radiation correction.

Compared to the combined Hulsbosch and Wakker (1988) plus Morras et al. (2000) survey, the LAB survey has advantages and disadvantages for the study of the HVCs. The LAB survey allows more detailed mapping (on a $0.5^\circ \times 0.5^\circ$ grid instead of a $1^\circ \times 1^\circ$ grid), has better velocity resolution (1.25 km s^{-1} vs 16 km s^{-1}), and it covers the IVCs. However, since the integration times for the LAB survey were much shorter than what was the case for the older surveys, the 5σ detection limit for a cloud with line width 20 km s^{-1} is about $3 \times 10^{18} \text{ cm}^{-2}$, slightly worse than in the Hulsbosch and Wakker (1988) survey. To achieve the same sensitivity in the LAB data therefore requires smoothing to a 1° beam. Thus, the ~ 150 small, faint ($< 1^\circ$ diameter; $T_{B,\text{peak}} < 0.08 \text{ K}$; $N(\text{HI}) < 3 \times 10^{18} \text{ cm}^{-2}$) clouds in the Hulsbosch and Wakker (1988) survey are below the LAB detection limit. Similarly, the faint edges of the large HVC complexes are more easily seen in the older survey. A combination of the old HVC surveys and the LAB data is therefore necessary to extract the most information.

🔗 *Figure 12-1* presents an all-sky map of the HVCs as seen in the combined Hulsbosch and Wakker (1988) and Morras et al. (2000) lists. Clouds in grey have $|\nu_{\text{LSR}}| > 90 \text{ km s}^{-1}$, but $|\nu_{\text{DEV}}| < 90 \text{ km s}^{-1}$, meaning that they should properly be classified as IVCs. 🔗 *Figures 12-2* and 🔗 *12-3* give a map of the IVCs at positive and negative velocities, based on the LAB survey. Detailed maps of many individual HVC and IVC clouds can be found in Wakker (2001) and Wakker et al. (2008).

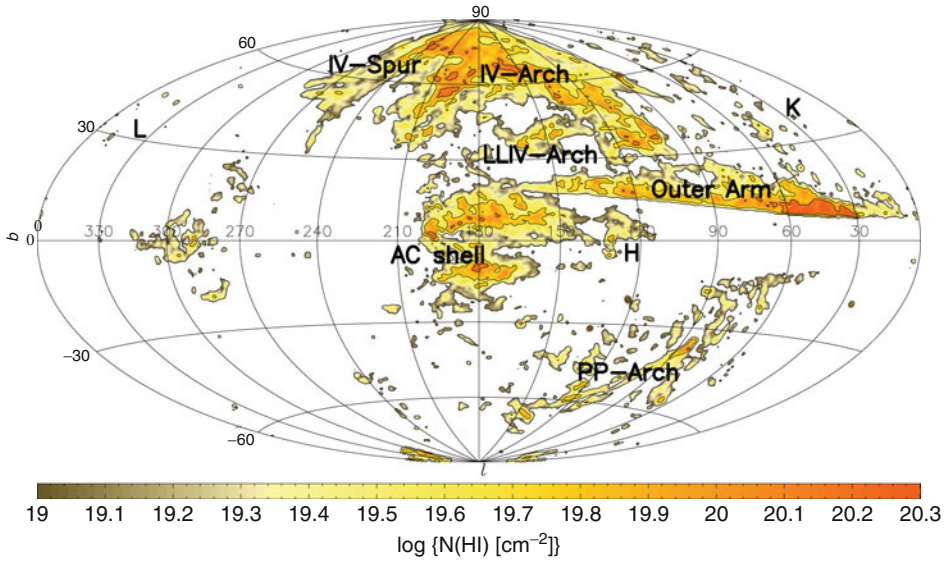
An improvement in the mapping of HVCs will be possible using some recent surveys. The Parkes GASS survey (Kalberla et al. 2010) provides data for $|\nu_{\text{LSR}}| < 468 \text{ km s}^{-1}$ at



■ Fig. 12-1

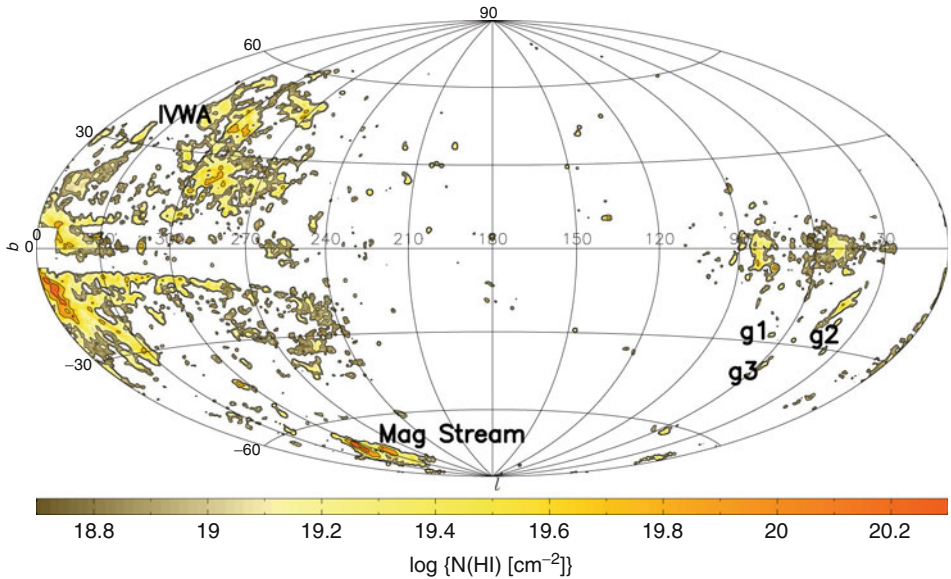
Aitoff projection all-sky map of the HVCs, in galactic coordinates, with the Anti-Center in the middle (Based on Hulsbosch and Wakker (1988) and Morras et al. (2000)). Contour levels are at brightness temperatures of 0.05 and 0.5 K. Colors code deviation velocities, with the scale given by the bar at the bottom. HVCs were selected using $|v_{\text{LSR}}| > 90 \text{ km s}^{-1}$. Gray clouds have $|v_{\text{LSR}}| > 90 \text{ km s}^{-1}$, but $|v_{\text{DEV}}| < 90 \text{ km s}^{-1}$. Labels give the names of the cloud complexes

declinations $< +1^\circ$ with a $14.4'$ beam and 0.057 K rms in a 1.0 km s^{-1} channel. The sky north of -5° declination will be covered by the Effelsberg HI survey (EBHIS; Winkel et al. 2010) on a $9.5'$ grid with 0.09 K rms per 1.25 km s^{-1} channel. The Arecibo GALFA-HI survey (Peek et al. 2011) covers the sky between declinations -1° and $+38^\circ$ with a $3.4'$ beam, 0.18 km s^{-1} channels, and rms 0.08 K in a 1 km s^{-1} channel. For HVCs with line widths 20 km s^{-1} , these surveys thus have single-beam 5σ detection limits of 2.5×10^{18} , 4.4×10^{18} , and $3.5 \times 10^{18} \text{ cm}^{-2}$, respectively. For a beam-filling cloud that is larger than $36'$ in size, smoothing to a $36'$ equivalent beam can potentially reduce this further to 1.0×10^{18} , 1.1×10^{18} , and $0.35 \times 10^{18} \text{ cm}^{-2}$, respectively. However, most faint clouds are small and/or have structure, so that in practice the faintest detections will have column densities larger than these numbers. Thus, compared to the LAB data, these surveys will allow making maps with increased angular resolution (by factors of 2.5, 3.8, and 10.6, respectively). However, for mapping the extended outer parts of the HVCs and searching for faint clouds, these new surveys are not much more sensitive than the combined Hulsbosch and Wakker (1988) and Morras et al. (2000) datasets, even after smoothing to the equivalent 16 km s^{-1} and $36'$ resolution.



■ Fig. 12-2

Aitoff projection all-sky map of the column density of the intermediate-velocity gas with deviation velocity between -90 and -35 km s^{-1} , based on the LAB survey (Kalberla et al. 2005). For clarity the resolution was degraded to 2° . Contours are shown at column densities of 10 , 50 , and $120 \times 10^{18} \text{ cm}^{-2}$. Labels give the names of the cloud complexes



■ Fig. 12-3

Aitoff projection all-sky map of the column density of the intermediate-velocity gas with deviation velocity between $+35$ and $+90 \text{ km s}^{-1}$, based on the LAB survey (Kalberla et al. 2005). For clarity the resolution was degraded to 2° . Contours are shown at column densities of 5 , 10 , 50 , and $120 \times 10^{18} \text{ cm}^{-2}$. Labels give the names of the cloud complexes

2.3 Features of the HVC Sky

Wakker and van Woerden (1991) used the HVC surveys of Hulsbosch and Wakker (1988) and Bajaja et al. (1985) to construct a catalogue of individual clouds, containing 561 objects. Since these surveys did not have full sky coverage (having $1^\circ \times 1^\circ$ and $2^\circ \times 2^\circ$ grids, respectively), many southern clouds and some small northern clouds were not included.

A noticeable feature of the HVC and IVC sky is that the high-velocity gas appears to concentrate in large clouds and complexes of clouds. Historically, these have been given names that are either descriptive or consist of letters. A, B, and C were the first discovered HVCs (B is now considered part of A); M, H, and K were named after their discoverers (Mathewson, Hulsbosch, Kerr); R was one of a series of features in a paper on outer Galactic spiral arms; GCP (also known as GP or as the “Smith Cloud”), GCN (or GN), and AC were named after their location in the sky (near the Galactic Center and Anti-Center); L was named after a constellation (Libra); D and G are close to C and H in the alphabet and in the sky; WA/WB/WC/WD/WE were so named because the complexes were discovered by Wannier, Wrixon and Wilson (1972) and catalogued by Wakker and van Woerden (1991); the Magellanic Stream appears related to the Magellanic Clouds; the Intermediate-Velocity Arch, Low-Latitude Intermediate-Velocity Arch and Pegasus-Pisces Arch (IV, LLIV, PP) were named by Kuntz and Danly (1996) and Wakker (2001) for their curved appearance. Finally, “gp” is the intermediate-velocity gas near the HVC complex “GP”, with the names “g1”, “g2” and “g3” for the three main clouds. Although in the main these complexes are well-defined, near their edges the exact outlines are sometimes vague. Further, for many small clouds their relation to a complex can be ambiguous.

For each cloud the following useful quantities can be observed: (a) (l, b, v_{LSR}) , the location and average velocity of the gas; (b) Ω , the cloud area; (c) σ , the dispersion between the velocities in the various directions toward which the cloud is seen; (d) T_{peak} , the brightness temperature of the brightest spot in the cloud; and (e) $m(\text{HI})$, the mass of the cloud assuming a distance of 1 kpc. $m(\text{HI}) [M_\odot \text{kpc}^{-2}] = 0.236 S [\text{Jy km s}^{-1}]$, with S the 21-cm flux integrated over velocity (see [Chap. 11](#) by Dickey in this volume). The actual HI mass is calculated from the relation $M(\text{HI}) = m(\text{HI}) D^2 M_\odot$, where D is the distance to the cloud in kpc. The conversion between brightness temperature ($T_B(v)$) and flux ($S(v)$) is given by $T_B(v) = \frac{\lambda^2}{2k} \frac{S(v)}{\omega}$, with ω the solid angle of the main telescope beam. For a gaussian velocity profile the integrated flux is $S = 1.064 S_{\text{peak}} W$, where W is the full-width-at-half-maximum (FWHM), and the factor 1.064 is really $\sqrt{\pi/4 \ln 2}$. Thus, for the Dwingeloo telescope (used for the LAB survey and having $\omega \sim (4\pi/8 \ln 2) (0.6^\circ)^2$), $m(\text{single beam}) \sim 78 T_{B,\text{peak}} (W/20 \text{ km s}^{-1}) M_\odot \text{kpc}^{-2}$.

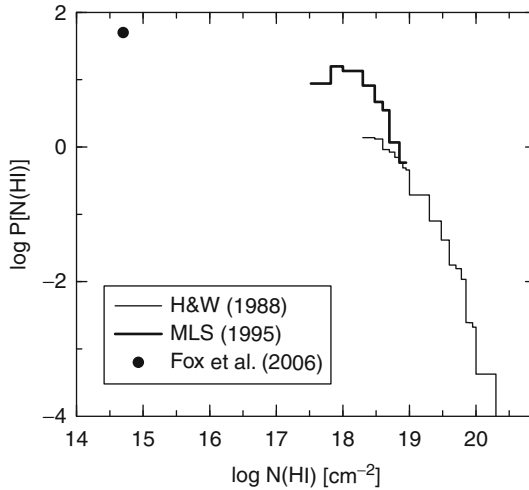
Wakker and van Woerden (1991) showed that although there are clearly recognizable HVC complexes, the distribution of the areas of individually defined clouds follows a power-law. That is, the number of clouds with area $>\Omega$ as function of area (Ω in square degrees) is

$$\log N(>\Omega) = -0.70 \log \Omega + 2.75$$

(using the updated values from Wakker 2004). Thus, for every 22 clouds with area >100 square degrees, there are 110 with area >10 square degrees, and 550 with area >1 square degree.

2.4 Sky Coverage

A question that is of substantial interest is toward how much of the sky high-velocity gas is seen. Giovanelli (1980) was the first to address this. Wakker (1991) studied it using the all-sky survey, and revisited it later (Wakker 2004). As [Figs. 12-1](#) and [12-4](#) show, the sky



■ Fig. 12-4


Percentage P of sky covered by HI with $v_{\text{DEV}} > 90 \text{ km s}^{-1}$. HI is binned in intervals of 10^{18} cm^{-2} for $N(\text{HI}) < 10^{19} \text{ cm}^{-2}$. For $N(\text{HI})$ between 10^{19} and 10^{20} cm^{-2} , the binning is in intervals of 10^{19} cm^{-2} , but the result is divided by 10. For $N(\text{HI})$ between 10^{20} and 10^{21} cm^{-2} , the binning is in intervals of 10^{20} cm^{-2} , but the result is divided by 100. This effectively makes all bins 10^{18} cm^{-2} wide, but smoothes out the sparsely populated bins at high column densities. The horizontal scale then displays $\log N(\text{HI})$ (see Wakker 2004 for a justification and more detailed explanation for using this kind of binning). The vertical scale gives the percentage of sky cover derived from three different datasets. The *thin solid histogram* is for data from Hulsbosch and Wakker (1988), the *thick solid histogram* for data from Murphy et al. (1995; MLS), while the large dot corresponds to the sky coverage seen in far-UV absorption by Fox et al. (2006)

coverage of gas with $|v_{\text{DEV}}| > 90 \text{ km s}^{-1}$ is substantial. In fact, HVC gas with $N(\text{HI}) > 10^{18} \text{ cm}^{-2}$ is seen toward 10% of the sky, most of it at negative velocities (7% vs 3% at positive velocities). Bright high-velocity gas ($N(\text{HI}) \gtrsim 10^{20} \text{ cm}^{-2}$) is rare, however, being seen in just $\sim 100 \text{ } 0.5$ beams (0.06% of the sky). On the other hand, fainter high-velocity gas ($N(\text{HI}) > 2 \times 10^{18} \text{ cm}^{-2}$) is seen toward 18% of the sky. No all-sky 21-cm surveys exist for even fainter clouds, but there are deep observations in both 21-cm and UV absorption in sightlines toward AGNs (QSOs and Seyfert galaxies). In particular, Murphy et al. (1995) observed 171 such directions. Using the detection fraction of high-velocity gas in that sample, Wakker (2004) estimated that the sky covering factor of HVCs with $N(\text{HI}) > 7 \times 10^{17} \text{ cm}^{-2}$ is 30%. The column density distributions found from the Hulsbosch and Wakker survey (1988) and implied by the Murphy et al. (1995) data are shown in ► Fig. 12-4.

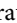
Also included in that figure is an estimate of the sky coverage at much lower column densities, based on observations made using the Far-Ultraviolet Spectroscopic Explorer (FUSE). Sembach et al. (2003) detected high-velocity O VI absorption in 59 of 102 ($\sim 60\%$) sightlines to AGNs. O VI was seen in almost every direction where 21-cm HI emission was previously known, but also in many other sightlines. Fox et al. (2006) showed that 75% of the

O VI detections also show detectable H I in the Lyman absorption lines, with column densities down to $10^{14.7} \text{ cm}^{-2}$. They further find that the sky covering fraction of high-velocity H I with $N(\text{H I}) > 5 \times 10^{14} \text{ cm}^{-2}$ is on the order of 50%.

2.5 HVC Kinematics

A noticeable feature of  Fig. 12-1 is that at $0^\circ < l < 180^\circ$ most HVCs have negative deviation velocities, while at $180^\circ < l < 360^\circ$ most values of v_{DEV} are positive. This is even more pronounced when v_{LSR} is used (see Wakker 1991, Fig. 3a; Wakker and van Woerden 1991, Fig. 2b). This velocity asymmetry is caused by a combination of two effects. First, the LSR moves at 220 km s^{-1} toward $l = 90^\circ$, $b = 0^\circ$, so that clouds in that direction that are not participating in Galactic rotation tend to have negative velocities. Second, relative to the Milky Way as a whole, the maximum velocity of HVCs appears to be about 250 km s^{-1} (see below). Thus, a cloud near $l = 90^\circ$ that is receding from the Milky Way at $+250 \text{ km s}^{-1}$ will have an apparent observed velocity of $+30 \text{ km s}^{-1}$, and it will not be classified as an HVC. On the other hand, a cloud at $l = 90^\circ$ that is at rest relative to the Milky Way will appear as a HVC with $v = -220 \text{ km s}^{-1}$.

These two properties imply that the population of HVCs must be extended relative to the size of the Milky Way, and that on average the clouds are not taking part in Galactic rotation. If the clouds were local (distances less than a few kpc), their peculiar velocities would be very large relative to the denser material in the disk. If the total spread in velocities were larger than $\pm 300 \text{ km s}^{-1}$, negative velocity clouds would become visible near $l = 270^\circ$, and positive-velocity clouds would be seen near $l = 90^\circ$.

This effect is illustrated in  Fig. 12-5. The open circles in the left-hand panel show the longitude- v_{LSR} distribution of the clouds with $|v_{\text{DEV}}| > 80 \text{ km s}^{-1}$ in the Wakker and van Woerden (1991) catalogue. The solid points are the locations predicted from a simple model of the distribution of cloud locations and velocities, with red points for the 400 clouds that would observationally be classified as a HVC and blue points for the 447 objects in the population that are hidden by low-velocity emission. The panel on the left shows two observables and the panel on the right gives the locations and velocities projected onto the Galactic plane. The model has the following characteristics: (a) space density proportional to R^{-2} out to $R = 80 \text{ kpc}$ (with R the distance to the Galactic Center); (b) randomly oriented transverse velocity given by the Galactic potential at its location, such that the radial gravitational force is balanced by the centrifugal force; this velocity is on the order of $200\text{--}250 \text{ km s}^{-1}$; (c) a random transverse and radial velocity component that has a distribution with dispersion 50 km s^{-1} ; (d) a radial infall component of 50 km s^{-1} ; and (e) a similar population surrounds M 31 (see below).

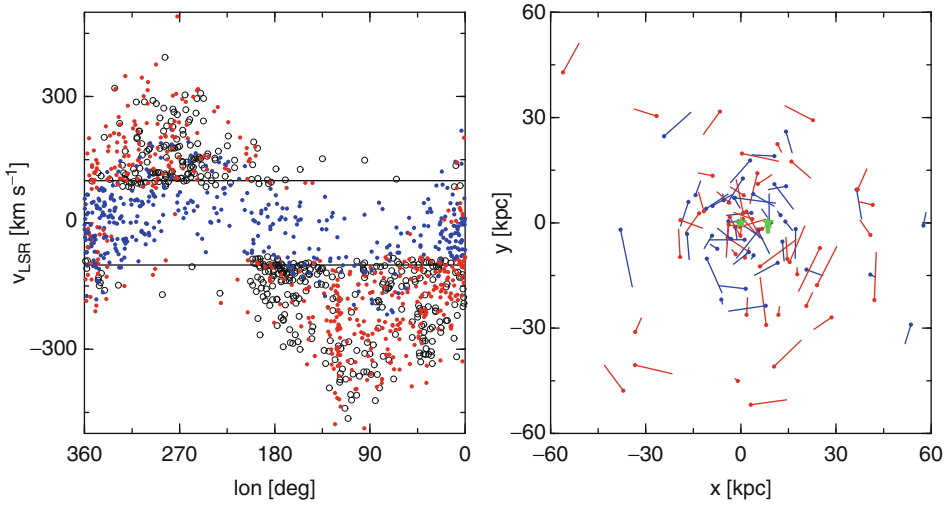
Defining a coordinate system (x, y, z) with the Galactic plane as the (x, y) plane and the Sun at $y = 0$, a cloud has a spatial location (x, y, z) and space velocity (v_x, v_y, v_z) , resulting in the following parameters:

$$r = \sqrt{x^2 + y^2}$$

$$d = \sqrt{(x - R_\odot)^2 + y^2 + z^2}$$

$$\Theta = \arctan \frac{y}{x}$$

$$l = \pi + \arctan \frac{y}{x - R_\odot}$$



■ Fig. 12-5

Left: comparison of observed and modeled distribution of the LSR velocity of HVCs as function of longitude. *Open circles* are for the clouds in the catalogue of Wakker and van Woerden (1991). *Red* and *blue* points are the predictions from the simple model described in the text, with red points for objects that would observationally be classified as a HVC. **Right panel:** locations and velocity vectors projected onto the Galactic plane for one fourth of the modeled clouds. The *green stars* give the locations of the Sun and of the Galactic Center

$$\begin{aligned}
 b &= \arcsin \frac{z}{d} \\
 v_r &= +v_x \cos \Theta + v_y \sin \Theta \\
 v_\Theta &= -v_x \sin \Theta + v_y \cos \Theta \\
 \sin \alpha &= \frac{R_\odot}{r} \sin l \\
 \cos \alpha &= \frac{r^2 + d^2 - R_\odot^2}{2rd} \\
 v_{\text{GSR}} &= (v_r \cos \alpha - v_\Theta \sin \alpha) \cos b + v_z \sin b \\
 v_{\text{LSR}} &= v_{\text{GSR}} + 220 \sin l \cos b,
 \end{aligned}$$

where r , d , Θ , and α are intermediate variables that go into the calculation of v_{GSR} (the cloud's velocity relative to the Galactic Center in a coordinate system in which the Milky Way rotates) and v_{LSR} (the cloud's velocity relative to the LSR).

The clouds can be given a mass based on a power-law mass spectrum:

$$N(M)dM = N_o M^\alpha dM; \quad M_{\text{low}} < M < M_{\text{upp}},$$

with $\alpha = -1.5$, as found by Wakker and van Woerden (1991). The upper mass limit is $10^7 M_\odot$, which is the mass found for HVC complex C (see ● Sect. 3). By assuming a constant density, n , the mass can be converted into a linear and angular size, which then allows deriving a brightness temperature. For the large, comparatively nearby HVCs typical densities of $0.05\text{--}0.15 \text{ cm}^{-3}$ are

found (see ● Sects. 2.6 and ● 4.3). For the more distant, less massive clouds that are embedded in a medium with lower pressure, a value of 0.01 cm^{-3} is more appropriate. Then:

$$\begin{aligned}
 R &= \left(\frac{3M}{4\pi m_a \bar{n}} \right)^{1/3} = 0.92 \left(\frac{M}{10^6 M_\odot} \right)^{1/3} \left(\frac{\bar{n}}{0.01 \text{ cm}^{-3}} \right)^{-1/3} \text{ kpc} \\
 \Omega &= \pi \left(\frac{R}{D} \right)^2 = \pi (318 \text{ arcmin})^2 \left(\frac{M}{10^6 M_\odot} \right)^{2/3} \left(\frac{\bar{n}}{0.01 \text{ cm}^{-3}} \right)^{-2/3} \left(\frac{D}{10 \text{ kpc}} \right)^{-2} \\
 S &= \frac{M(\text{HI})}{0.236 D^2} = \frac{2k}{10^{-26} \lambda^2} \sqrt{\frac{\pi}{4 \ln 2}} W T_{\text{B,p}} \Omega \Rightarrow \\
 T_{\text{B,p}} &= 0.59 \left(\frac{f}{0.5} \right) \left(\frac{M}{10^6 M_\odot} \right)^{1/3} \left(\frac{\bar{n}}{0.01 \text{ cm}^{-3}} \right)^{2/3} \left(\frac{W}{20 \text{ km s}^{-1}} \right)^{-1} \left(\frac{\min(\Omega, \Omega_{\text{beam}})}{\Omega_{\text{beam}}} \right) \text{ K}.
 \end{aligned}$$

Here M is the cloud mass in M_\odot , f is the neutral fraction ($f = M(\text{HI})/M(\text{H})$), m_a the average particle mass (~ 1.23 times the mass of a hydrogen atom, taking into account helium and heavy elements), R the cloud radius in kpc, D its distance to the Sun in kpc, Ω the area in steradians, S the flux integrated over the profile in Jy km s^{-1} , $\lambda \sim 0.21 \text{ m}$ the wavelength, W the FWHM of the velocity profile in km/s , and T_{B} the brightness temperature in K. The factor Ω_{beam} accounts for beam dilution. If the cloud is resolved, then T_{B} does not depend on D , as the apparent cloud area Ω also contains a factor D^{-2} . However, for unresolved clouds (i.e., clouds smaller than the telescope's beam size) beam dilution reduces the observed brightness temperature.

The simple kinematical model shows that the velocity distribution of the HVCs can be explained by a population of clouds that generally orbit the Milky Way, but that are also falling in with a net velocity of 50 km s^{-1} . This determines the velocity range from about -250 to $+200 \text{ km s}^{-1}$ when measuring velocities relative to the Milky Way, and -450 to $+300 \text{ km s}^{-1}$ when measuring relative to the LSR. About half of the clouds in such a population would not be classified as a HVC. The infall shifts the distribution in the l - v_{LSR} diagram such that the most negative velocity near $l = 90^\circ$ is 100 km s^{-1} more negative than the most positive velocity near $l = 270^\circ$. By themselves, these properties of the distribution cannot be used to determine the radial extent of the population, as long as it is much larger than the distance of the Sun from the Galactic Center. However, assuming that M 31 is also surrounded by a similar population of clouds implies an upper limit on the radial extent of about 80 kpc , since otherwise there would be an obvious concentration of HVCs in the sky area around M 31. Even in the model shown in ● Fig. 12-5, about 25 of the clouds are actually orbiting M 31. The detection of HVC-like objects near M 31 (Thilker et al. 2004) lends support to this picture of the HVCs.

2.6 Ionized HVCs

Not all of the hydrogen in HVCs and IVCs is in neutral form. In fact, it appears that H^+ represents a large fraction. This is to be expected, as can be shown by considering an atomic hydrogen layer of constant volume density n (in cm^{-3}) and fixed thickness (following Maloney 1993). First, define α , the hydrogen recombination coefficient ($\alpha = 2.6 \times 10^{-13} \text{ cm}^3 \text{ s}^{-1}$ for gas with $T \sim 10^4 \text{ K}$). Then, for a flux of ϕ ionizing photons $\text{cm}^{-2} \text{ s}^{-1}$ incident on both sides of this gas layer, there is a critical total hydrogen column density

$$N_c \sim \frac{2\phi}{\alpha n} = 7.7 \times 10^{18} \left(\frac{\phi}{10^{5.0}} \right) \left(\frac{n}{0.1} \right)^{-1} \text{ cm}^{-2},$$

below which the recombination rate ($\alpha n N_c$) is too small to balance the ionizing flux. Note that in the model of Bland-Hawthorn and Maloney (1999) $\log \phi = 4.5$ – 5.0 at galactocentric radii,

$R \sim 8\text{--}12$ kpc (for heights above the plane, z , up to 20 kpc); $\log \phi \sim 5.5$ at $R \sim 6$ kpc, $z < 10$ kpc; $\log \phi \sim 3.5$ at $R > 13$ kpc. Gas with column density $N < N_c$ will be mostly ionized, while gas with $N > N_c$ will be mostly neutral. The typical density of 0.1 cm^{-3} chosen above is based on the observed typical value in HVCs (see [Sect. 4.3](#)). The numerical value of the critical column density shows that most of the smaller, fainter HVCs probably are the central cores of larger, mostly ionized clouds. Mostly neutral gas is only expected to be present in the few percent of the sky covered by the brighter HVC cores.

In many circumstances, the H^+ can be observed by means of the $\text{H}\alpha$ photons that it emits. $\text{H}\alpha$ observations of HVCs are important for three reasons: First, they show the distribution of the ionized component of the clouds, which can be directly compared to the distribution of the neutral phase, revealing their full extent. Second, by combining $\text{H}\alpha$ and H I observations, it is possible to derive the volume density of a cloud. Adding data on the $[\text{S II}]$ optical emission line also allows the derivation of the temperature and pressure of a cloud. How to do this is described in [Sect. 4.3](#). Third, $\text{H}\alpha$ intensities contain information on the cloud distances and the intensity of the ionizing radiation surrounding the Milky Way; this is described in [Sect. 3.1](#).

Although $\text{H}\alpha$ emission has been detected in selected directions toward a number of individual clouds (Weiner and Williams 1996; Bland-Hawthorn et al. 1998; Tufté et al. 1998; Putman et al. 2003), maps are only available for two IVCs (complexes K and L – Haffner et al. 2001, 2005) and two HVCs (complex GP – Hill et al. 2009; complex A – Barger et al. 2012). An all-sky survey of HVC $\text{H}\alpha$ emission is not available, for two main reasons: First, to produce measurable $\text{H}\alpha$ emission requires gas with sufficient density, since the emission is proportional to the square of the density. Second, there are few instruments that have the sensitivity and velocity resolution to detect the HVCs, and the ones that exist have relatively narrow bandwidth, so that they need to be tuned to cover the range of velocities where high-velocity emission occurs.

3 The Determination of Cloud Distances and Metallicities

Two of the most important quantities that are used to understand the origin and properties of HVCs are their distance and their metallicity. Both of these are mainly derived from studies of absorption lines. This section describes the methods that are used to obtain information about HVC distances and metallicities.

By definition the HVCs do not take part in Galactic rotation. Therefore, it is not possible to combine their apparent velocity with a model of differential rotation to estimate a distance. Several different approaches have been proposed, which were summarized and critiqued in Wakker and van Woerden (1997) and in van Woerden and Wakker (2004). The most useful indirect techniques are first summarized, then the so-called absorption-line method is described in detail.

3.1 HVC Distances from Indirect Methods

3.1.1 $\text{H}\alpha$ Intensity

In principle the amount of $\text{H}\alpha$ emission coming from an HVC is a direct measure of the intensity of the ionizing radiation field, as on average each Lyman continuum photon is converted into $0.46\text{H}\alpha$ photons (see Spitzer 1998). Ferrara and Field (1994) work this out

in more detail, taking into account the confinement of HVCs by a surrounding medium, which affects the density structure, and thus the ionization structure and emission measure. Thus, in principle, if one has a prediction for the ionizing flux as function of location, then the observed H α emission measure directly gives the distance. Such a model was made by Bland-Hawthorn and Maloney (1999). However, when they applied their model to observations of the Magellanic Stream, they found that the observed H α emission was much stronger than was predicted, which means that an extra source of ionization is needed, or the model needs to be renormalized. Furthermore, for all HVCs that have been observed in multiple directions (complex K, L, GP, A, the Magellanic Stream), the observed H α intensity varies from point to point, which means that there are probably also geometrical (i.e., shadowing) effects due to small-scale structure in the clouds. It is more likely that in the end this method will be applied in reverse, to determine the intensity of the radiation field at different locations, using clouds with known distances.

3.1.2 Pressure Equilibrium

Since the clouds have a timescale for free expansion that is relatively short (see [Sect. 4.2](#)), they are either transient or confined by the pressure of a surrounding hot medium. Evidence for the latter comes from the detection of high-velocity O VI absorption, which is best interpreted as originating in an interface between the neutral cloud and a hot medium (see [Sect. 5](#)). Modeling the change of pressure with height above the Galactic plane can then give an estimate for the cloud's distance (Benjamin and Danly 1997; Espresate et al. 2002), giving values of a few kpc. However, the models are relatively simple and some of the necessary Galactic parameters are not well known.

3.1.3 Velocity Gradients

In a few larger clouds a velocity gradient is visible. Such gradients can be interpreted as due to projection effects, which then imply a distance. The most prominent case is that of the GCP complex, for which Lockman et al. (2008) find a distance of ~ 10 kpc, agreeing with the value derived from other methods. Using similar methods, Lockman (2003) derived a distance of 25 kpc for complex H.

3.1.4 The Virial Theorem

An easily derived quantity that suggests itself from the HVC observables (see [Sect. 2.3](#)) is the distance at which a cloud would be self-gravitating and in virial equilibrium. In that case

$$\sigma^2(3D) = \frac{2\alpha GM(\text{HI})}{fR},$$

where α is a factor near 1 that depends on the cloud geometry and virialization (Bertoldi and McKee 1992; see also Blitz et al. 1999); $\alpha = 1/2$ for a spherical cloud. f is the ratio of H I mass to total mass, including ionized and molecular hydrogen, helium and possible dark and stellar matter. For a cloud without dark or stellar matter in which hydrogen is 50% ionized,

$f = 0.5 * 0.748 = 0.374$, where 0.748 is the ratio $M(\text{H})/(M(\text{H})+M(\text{He})+M(\text{metals}))$. Converting the observables into the quantities in this formula ($\sigma(3D) = \sqrt{3} \sigma_{\text{obs}}$, $M(\text{HI}) = m(\text{HI}) D^2 = 0.236 S D^2 M_{\odot}$, $R = \sqrt{\Omega/\pi} D$) and rearranging yields:

$$D_{\text{vir}} = \frac{3}{2\pi^{1/2} \alpha} \frac{f \Omega^{1/2} \sigma_{\text{obs}}^2}{G m(\text{HI})} = 4500 \left(\frac{f}{0.374} \right) \left(\frac{\alpha}{0.5} \right)^{-1} \left(\frac{\Omega}{6sq^{\circ}} \right)^{1/2} \left(\frac{\sigma_{\text{obs}}}{10} \right)^2 \left(\frac{m(\text{HI})}{140} \right)^{-1} \text{ kpc}$$

A calculation of D_{vir} only makes sense for clouds that are detected in multiple beams. The typical mass of $140 M_{\odot}$ and typical area 6 square degrees are the median values for clouds with area >2 square degrees. Thus, the implied “virial distance” for a typical cloud is 4.5 Mpc.

The fact that such large distances are implied for clouds to be gravitationally stable if they only contain hydrogen used to be taken as an argument that they are unstable and transient (Hulsbosch 1975). Blitz et al. (1999), however, suggested that instead the HVCs are the visible part of the missing dark matter halos that are predicted to exist by cosmological simulations, with $f = 0.1$. They also assumed that a typical cloud structure gives $\alpha = 1$. This results in virial distances that are a factor ~ 10 smaller, on the order of a few 100 kpc, placing the HVCs in the Local Group. However, many more such halos are expected than the number of observed HVCs (see review by Kravtsov 2010).

Using this idea, Braun and Burton (1999) proposed that the small HVCs form a separate class, which they named the compact HVCs (CHVCs), which would be the Local Group objects, in contrast to the large, relatively nearby complexes. They mapped individual clouds in detail (see de Heij et al. 2002b and references therein), and in some cases interpreted the velocity field as due to rotation in a self-gravitating cloud. However, the area distribution of the HVCs follows a power law, suggesting that the CHVCs do not form a separate class. Further, not all CHVCs show a regular velocity field that can be interpreted as rotation.

In [Sect. 2.5](#) above, it was shown that the general population of HVCs is likely to have an extent of about 80 kpc, and that there are similar clouds associated with M 31. On the other hand, free-floating clouds with masses as large as those predicted in the Blitz et al. (1999) picture described above have not been detected in other galaxy groups that are similar to the Local Group, at least down to a detection limit of $4 \times 10^5 M_{\odot}$ (Zwaan 2001; Pisano et al. 2007). Maloney and Putman (2003) pointed out that, at distances on the order of 1 Mpc, the observed CHVCs would be so large that their HI densities would be on the order of $2 \times 10^{-4} \text{ cm}^{-3}$; hence, they would have to be predominantly ionized by the intergalactic radiation field, and their masses would be so great that the line widths would far exceed those observed. Thus, although many HVCs may be far from the Galactic plane, the population as a whole is unlikely to represent the missing dark matter halos at Local Group distances. This also implies that they likely are not self-gravitating, and thus some mechanism is required to hold them together.

3.2 Absorption-Line Method for Determining Distances

All methods listed above require major assumptions about the properties of the clouds and the Galactic environment, and they are not applicable in general. Statistically they might be useful, and they can be used as sanity checks. However, the only unambiguous results come from the “absorption-line method.” This method was described in several papers (Schwarz et al. 1995; van Woerden et al. 1999b; Wakker 2001). It requires the kinds of data described below.

3.2.1 Suitable Stellar Candidates Projected onto the HVC

A suitable type of star should be numerous at high galactic latitude, have a relatively reliable estimated distance, and have few stellar lines that can interfere with interstellar absorption. This leads one to Blue Horizontal Branch (BHB) stars, subdwarf B stars, and RR Lyraes. Before the year 2000 such stars were mostly found using low-resolution objective-prism spectra or photometric observations of individual stars (e.g., Kukarkin et al. 1970 – General Catalog of Variable Stars; Green et al. 1986 – the PG catalog; Beers et al. 1996 – the “HK” survey). At present, however, the great majority of candidate targets come from two surveys: 2MASS (Cutri et al. 2003), which provides JHK magnitudes for all objects in the sky down to magnitude $J \sim 15.5$, and the Sloan Digital Sky Survey (SDSS; York et al. 2000), which gives $ugriz$ magnitudes for QSOs and stars fainter than $g \sim 15$ in (mostly) the northern sky. Brown et al. (2004) determined the range of $J - H$ and $H - K$ colors of BHB stars from a sample of 550 spectroscopically observed halo stars, including 30 BHBs. They found that 65% of BHB stars have $-0.20 < (J - H)_o < 0.10$ and $-0.10 < (H - K)_o < 0.10$ and 41% of the stars in a sample selected using that criterion are BHBs. About 100,000 stars in the 2MASS survey fit these color criteria. In the case of the SDSS, there are several detailed studies that show how to use the $ugriz$ colors to select RR Lyrae and BHB candidates (Sirko et al. 2004; Ivezić et al. 2005). These studies yield a sample of 175,000 RR Lyrae and 15,000 BHB candidates, with about 85% accuracy. If a star was identified as a possible BHB or RR Lyrae, a preliminary distance can be estimated, using $M_V = 0.68$ for RR Lyraes (see [▶ Chap. 16](#) by Feast in this volume) and using the relation between absolute magnitude and color found by Preston et al. (1991) for BHBs. Next, these stars can be correlated with the high-velocity cloud catalogue to yield a list of stars at a range of distances in the direction of the HVCs.

3.2.2 Spectra and Photometry to Characterize the Candidates

It is possible to select the stars based on only their colors, but as the color-color selection is only about 75% accurate, it is necessary to obtain high-quality photometry and intermediate-resolution ($\sim 1 \text{ \AA}$) spectroscopy for a more detailed classification. The spectral shape, colors, and spectral features such as the width of the Balmer and Ca II H and K lines can then be matched against stellar atmosphere models to derive the stellar temperature, T_{eff} , gravity, $\log g$, and metallicity, Z . Comparing these numbers against theoretical isochrones (see e.g., Girardi et al. 2002) then yields an absolute magnitude. This also allows an estimate of the uncertainty in the absolute magnitude implied by the uncertainty in the stellar parameters.

3.2.3 High-resolution Spectra of Stars at Distances Bracketing that of the HVC

Absorption (by any ion) at the velocity of the HVC in the spectrum of a background star sets an upper limit on the cloud's distance, while a significant non-detection toward a foreground star sets a lower limit. A resolution of at least 15 km s^{-1} is needed, not only because that matches the typical width of the HVC absorption (thus optimizing the sensitivity), but also so that it is possible to separate the low- and high-velocity interstellar absorptions from each other and from stellar lines.

To convert a non-detection into a lower distance limit requires eliminating the possibility that it is due to too little HVC material in the direction of the star or to a low ionic abundance. This requires additional data: an accurate HI column density toward the star, and an accurate ionic abundance in the cloud. The latter can be obtained from a high-resolution spectrum of an extragalactic object or of a star known to lie behind the cloud, combined with good 21-cm data. The combination of a good ionic abundance and a good 21-cm column density allows a prediction of the equivalent width (EW) toward stars showing a non-detection. Then, as described by Wakker (2001), a lower distance limit follows if the ratio (predicted EW)/(observed 3σ EW limit) is larger than ~ 3 . For the UV lines of C II and Mg II the expected line strength is very large, with typical expected optical depth $\gg 1$, and spectra with low S/N ratio will suffice. However, this requires a telescope in space and the amount of available observing time is limited. For Ca II K (the best optical line; see [Sect. 3.4](#)), the typical expected equivalent width is 30–50 m Å, so a significant non-detection typically requires spectra with an equivalent width error of ~ 5 m Å, which requires an S/N ratio on the order of 50. Note that in the case of Ca II the typical expected equivalent width depends only very slightly on the HI column density (see [Sect. 3.4](#)).

To determine an upper distance limit to a cloud, it is sufficient to measure the equivalent width of an absorption line, which can be derived by a straight integration of the line profile:

$$W = \int_{\lambda_{\min}}^{\lambda_{\max}} \left(1 - \frac{F_{\lambda}}{C_{\lambda}}\right) d\lambda,$$

where F_{λ} is the observed flux, C_{λ} is the continuum flux, $d\lambda$ the wavelength step, and $\lambda_{\min/\max}$ are the wavelengths corresponding to the velocity range of the absorption.

To interpret non-detections requires an upper limit on the equivalent width, given by for example, three times the error. The total error in the equivalent width contains several contributions: photon counting noise, sky background, read-out error, dark current, the continuum fit, fixed-pattern noise, and uncertainties in the integration range. Spectroscopic calibration pipelines usually provide an error in the observed flux which combines the first four of these items. To convert this into an equivalent width error requires assuming a wavelength range over which to integrate, as the error is proportional to the square root of the integration range. The optimal choice is to match the width of the HVC 21-cm emission, typically 15–25 km s⁻¹. Combining in quadrature the flux errors with the errors in the continuum fit then gives a “statistical error.” The fixed-pattern error and the velocity-limits error can be combined in quadrature into a “systematic error.” In principle such a systematic error should also include uncertainties in the oscillator strength of the absorption line, but this is often ignored, and is usually relatively small. The statistical error indicates how accurately the measurement can be made, while the systematic error indicates how much the listed equivalent width could be offset from the actual value due to uncertainties associated with unknown but nonrandom offsets.

3.3 Considerations for Metallicity Measurements

In principle, measuring the metal content of a HVC is as simple as taking the ratio of the column density of a heavy element to the hydrogen column density. In practice there are the following items to take into account.

3.3.1 HI Small-Scale Structure

Heavy element column densities are usually measured by means of ionic absorption against background targets, most of which are QSOs or Seyfert galaxies (i.e., Active Galactic Nuclei or AGNs). Thus, there is a mismatch in angular sampling between the gas seen in absorption in the pencil-beam against the AGN and the gas seen in 21-cm emission using a radio telescope. This is minimized by taking radio spectra with the smallest possible beam, preferably using an interferometer such as the Westerbork telescope (WSRT), the Very Large Array (VLA), or the Australia Telescope (ATCA), which achieve beams of $<1'$. However, HVCs are often too faint to be detected by these interferometers. The Arecibo dish yields spectra with $3'$ resolution, but can only see part of the sky. The Green Bank, Effelsberg and Parkes telescopes have $\sim 10'$ – $15'$ beams, while the LAB survey covers the whole sky at $36'$ resolution. Wakker et al. (2001, 2011) find that using the LAB data yields column densities that are accurate to $\sim 25\%$, while using a $10'$ beam reduces the uncertainty to about 10%.

3.3.2 Depletion onto Dust

Dust is a ubiquitous constituent of the ISM, and its presence implies that the gas-phase column density measured for a heavy element does not represent the total column density. Savage and Sembach (1996) review this at length, comparing depletion in cold disk, warm disk, and halo gas, and they conclude that dust takes out fewer atoms in halo gas than in disk gas. However, except for oxygen and sulfur, depletion remains an issue. Where sulfur appears to avoid dust grains, oxygen will still be in the grains, but its large abundance means that most of the oxygen remains in the gas phase. In some circumstances silicon can also be useful, since in diffuse halo gas its abundance reduction is usually less than a factor 2. It should be noted that Savage and Sembach (1996) used measurements toward the IV-Arch and the PP-Arch to represent the halo gas. Note further that although dust is a problem when trying to estimate the metallicity of a cloud, estimates of the amount of dust in HVCs provide clues to their origin (see [Sect. 4.4](#)).

3.3.3 Presence of Ionized Hydrogen

As discussed in [Sect. 2.6](#), not all of the hydrogen in HVCs is neutral. To derive a metallicity therefore also requires an estimate of the relative content of ionized hydrogen, which is possible by measuring the cloud's $H\alpha$ emission, or by applying a photo-ionization model. Both of these methods require a distance estimate for the cloud, since the $H\alpha$ emission is proportional to the square of the density and the pathlength through the cloud, and the intensity of the ionizing radiation field depends on the cloud's location.

3.3.4 Elemental Ionization Fractions

In the diffuse ISM the balance between photoionization and recombination leads to a situation where most elements mainly occur in one dominant ionization state. Which state that is is

determined by the first ionization potential of the element that is larger than that of hydrogen, 13.6 eV. The relevant ionization potentials of sulfur, silicon, and iron are 10.36 eV ($S^0 \Rightarrow S^+$), 23.33 eV ($S^+ \Rightarrow S^{+2}$), 8.15 eV ($Si^0 \Rightarrow Si^+$), 16.35 eV ($Si^+ \Rightarrow Si^{+2}$), 7.87 eV ($Fe^0 \Rightarrow Fe^+$), 16.18 eV ($Fe^+ \Rightarrow Fe^{+2}$), which usually results in >90% of these three elements being in the form of S^+ , Si^+ , and Fe^+ in gas with total column density $>10^{18.5} \text{ cm}^{-2}$ (see next section). Since absorption lines from S^+ , S^{+2} , Si^+ , Si^{+2} , Fe^+ , and Fe^{+2} are all observable, this can often be checked observationally. Oxygen has an ionization potential that is close to that of hydrogen (13.62 eV for O^0 vs 13.60 for H^0), leading to a charge-exchange reaction that couples the column densities of O I and H I (Osterbrock 1989). This makes O I/H I the most reliable measure, as no correction is needed for the presence of O^0 , O^{+2} , or H^+ . That is, the fraction of ionized hydrogen and oxygen no longer matters, and the measured O I/H I ratio is only affected by dust depletion and small-scale structure (since the O I is measured in a pencil-beam, while H I is measured with a much larger 21-cm beam).

3.4 Strength of the Absorption Lines

The detectability of absorption lines from a given interstellar ion is determined by a combination of factors, including the element's cosmic abundance (A), the fraction of the element left in the gas phase after depletion onto interstellar dust grains (δ), the fraction of the element in a given ionization stage (F), and the oscillator strengths (f) and wavelengths (λ) of the absorption lines of the particular ion. Given a total hydrogen column density $N(H)$ (i.e., combining the neutral, ionized, and molecular phases) and an FWHM, W , the optical depth $\tau(\nu)$ as function of velocity associated with a given absorption line will be:

$$\tau(\nu) = \frac{\pi e^2}{m_e c} f \lambda_0 F \delta A N(H) \Phi(\nu)$$

where $\Phi(\nu)$ gives the absorption profile, normalized to have an integral of 1. That is, for a gaussian line profile the peak value of Φ , $\Phi(0)$ equals $1/(W \sqrt{\pi/4 \ln 2}) = 1/(1.064 W)$. The product $\frac{\pi e^2}{m_e c}$ has the value 2.654×10^{-2} in cgs units. Conventionally, however, λ is expressed in \AA , $N(H)$ in cm^{-2} , W in km s^{-1} , and Φ in $(\text{km s}^{-1})^{-1}$, in which case the coefficient has the value 2.654×10^{-15} .

• **Table 12-1** presents a simple estimate of the predicted optical depths and equivalent widths for a number of spectral lines given gas with solar abundance and total $N(H) = 10^{19} \text{ cm}^{-2}$ (assuming $W = 15 \text{ km s}^{-1}$). The lines listed include the most important lines in the far UV (O I, C II, Si II) and near UV (Mg II), which have been observed using the spectrographs on the Hubble Space Telescope. Also shown are results for the four strongest lines in the optical (the Ca II and Na I doublets).

The table shows that the UV lines of C II, Si II, and Mg II will typically saturate for H I column densities above $\sim 10^{18} \text{ cm}^{-2}$, making them easy to detect and in principle ideal to derive distance brackets for clouds. However, distant stars are usually too faint in the UV to observe with current space spectrographs. In the optical, the Ca II lines have an expected optical depth on the order of 0.1–0.5, making it possible to detect them in data with sufficiently high S/N ratio (>50). Note that Na I has not been detected in any HVC; considering the low expected optical depth this is not surprising.

■ Table 12-1

Relative strengths of absorption lines

Ion (1)	λ (Å) (2)	f (3)	$\log \delta$ (4)	$\log F$ (5)	$\log A$ (6)	τ_0 (7)	EW (m Å) (8)
O I	1302.169	0.0504	0.0	0.0	-3.31	53.4	165
O I	1039.230	0.00904	0.0	0.0	-3.31	7.65	98
C II	1334.708	0.1278	-0.30	0.0	-3.57	38.2	163
C II	1036.337	0.118	-0.30	0.0	-3.57	27.4	121
Mg II	2796.352	0.629	-0.38	0.0	-4.40	48.5	352
Mg II	2803.531	0.314	-0.38	0.0	-4.40	24.3	323
Si II	1260.442	1.070	-0.27	0.0	-4.49	38.9	158
S II	1250.584	0.00545	0.0	0.0	-4.88	0.149	9
S II	1253.811	0.01088	0.0	0.0	-4.88	0.299	18
S II	1259.519	0.01624	0.0	0.0	-4.88	0.448	26
Ca II	3934.777	0.6346	-1.0	-0.7	-5.66	0.181	36
Ca II	3969.591	0.3145	-1.0	-0.7	-5.66	0.091	19
Na I	5891.583	0.670	-1.0	-1.7	-5.76	0.023	7.1
Na I	5897.558	0.335	-1.0	-1.7	-5.76	0.011	3.6

Notes: Col. 1: Ion. Col. 2: Wavelength of line. Col. 3: Oscillator strength, from Morton (2003). Col. 4: Typical depletion for elements in the warm ISM; from Savage and Sembach (1996); for carbon, it is assumed that 50% is in dust. Col. 5: Typical ionization fraction for elements in the warm ISM at $N(\text{HI}) \sim 10^{19} \text{ cm}^{-2}$; these are implied by a calculation using the “CLOUDY” photoionization code (Ferland 1996); for O, C, Mg, Si, and S, F is generally ~ 1 , except in very low-density material ($n < 0.01 \text{ cm}^{-2}$), in high radiation fields ($\phi > 10^6 \text{ ph cm}^{-2} \text{ s}^{-1}$), and/or at low column densities ($N(\text{HI}) < 10^{19} \text{ cm}^{-2}$), where variations up to a factor 10 are possible; the value for Ca II is based on the empirical relation between the Ca II abundance and $N(\text{HI})$, using $N(\text{HI}) = 10^{19} \text{ cm}^{-2}$. Col. 6: Solar elemental abundance, from Asplund et al. (2009). Col. 7: Optical depth in the line center for an HI column density of 10^{19} cm^{-2} , assuming an intrinsic line width of 15 km s^{-1} and assuming solar abundances. Col. 8: Equivalent width of line for a total hydrogen column density of 10^{19} cm^{-2} .

● Figure 12-6 presents a closer look at how the ionization of the important ions O I, S II and Ca II depends on the environment. This figure was created using the “CLOUDY” photoionization code (Ferland 1996). Column densities were calculated for a plane parallel layer, illuminated from one side, for a series of assumed volume densities ($n = 0.01\text{--}1 \text{ cm}^{-3}$) and several radiation fields (ϕ). In particular ϕ was chosen to represent the environment near the Sun (see caption). The spectral shape of the Milky Way radiation field was taken from Fox et al. (2004).

The figure shows that for a cloud located above the Galactic plane that has $N(\text{HI}) > 10^{18.0} \text{ cm}^{-2}$, all oxygen is in the form of O I, with deviations only occurring in intense radiation fields ($\log \phi > 6$), which could happen for an IVC with low HI column density that is close to the Galactic plane. For most HVCs the observed O I/H I ratios in HVCs lie below this line, showing that they have subsolar metallicity.

For sulfur, ● Fig. 12-6 shows that ionization corrections may become important when $N(\text{HI}) < 10^{19.0} \text{ cm}^{-2}$, but only in low-density gas ($\log n < -1.0$) or in strong radiation fields ($\log(\phi/n) > 5$). Thus, the low S II/H I ratios that are observed in high column density HVCs indicate subsolar metallicity. In clouds with low $N(\text{HI})$ the situation is more complex. Fortunately, it is possible to use the S III $\lambda 1012.501$ line to assess this: if the physical conditions are

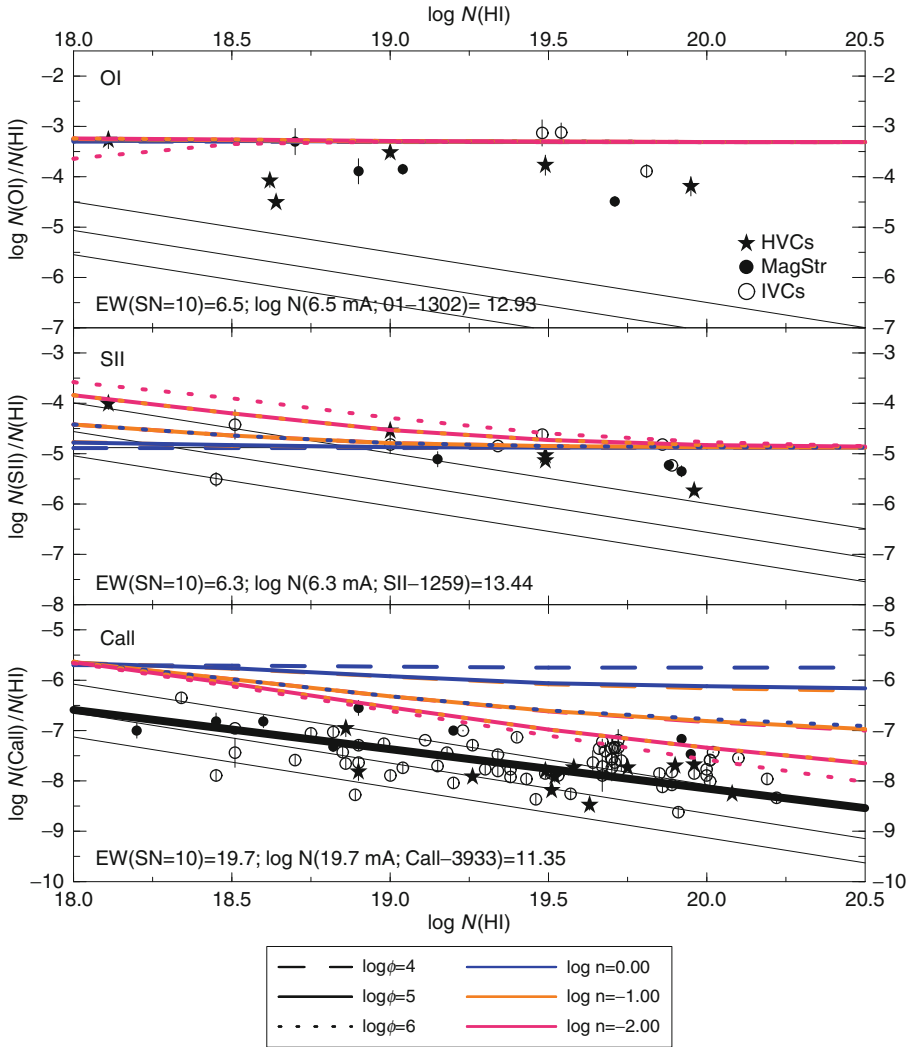


Fig. 12-6

Predicted apparent abundance ($N(\text{ion})/N(\text{H I})$) for O I, S II, and Ca II, as function of HI column density. Calculated using the “CLOUDY” photoionization code (Ferland 1996), for a plane parallel layer and assuming solar metallicity gas. *Solid lines* are for an ionizing radiation field intensity $\phi = 10^5 \text{ ph cm}^{-2} \text{ s}^{-1}$, corresponding to clouds at the solar circle with heights up to 20 kpc. *Dashed lines* are for $\phi = 10^4 \text{ ph cm}^{-2} \text{ s}^{-1}$, corresponding to locations outside the solar circle (from $R = 11 \text{ kpc}$, $z = 0 \text{ kpc}$ to $R = 18$ at $z = 10 \text{ kpc}$). *Dotted lines* are for a higher-intensity field in the plane and closer to the Galactic center (at $R \sim 3 \text{ kpc}$, $z < 3 \text{ kpc}$). Colors correspond to different volume densities. The *solid and dashed red lines* most likely represent the situation for HVCs. The observed values in HVCs, the Magellanic Stream and IVCs are given by filled stars, filled circles and open circles, respectively. Note that the observed O I and Ca II values lie below the colored model lines, which is due to the subsolar metallicity of the clouds in the case of O I, and due to depletion onto dust grains for Ca II. The three diagonal lines show the abundances corresponding to central optical depths of 1 (*top*), 0.1 (*middle*) and 0.03 (*bottom*), assuming a FWHM of 15 km s^{-1} . The *thick black line* in the Ca II panel is the empirical fit of Wakker and Mathis (2000)

such that $S\text{ II}/H\text{ I} > S/H$, then the S III line becomes detectable, and the S II/S III ratio can be used to determine the ionization corrections.

The behavior of Ca II differs from that of oxygen and sulfur because the ionization potentials of both Ca^0 and Ca^+ are less than 13.6 eV. Therefore, in gas with high H I column density, Ca^{+2} is the dominant ion, while Ca II/H I appears to be subsolar. In gas with low $N(\text{H I})$, Ca^{+2} is still the dominant ion at low volume densities, but Ca^+ is dominant at high volume density. The balance works out such that for $\log N(\text{H I}) < 18.3$ Ca II/H I is always about equal to Ca/H. For higher values of $N(\text{H I})$ a different situation can prevail, where in low density gas and/or high radiation intensity ($\log n < -1.5$ and $\log \phi > 4.5$) the Ca II column density varies by less than 0.4 dex for $\log N(\text{H I})$ between 18.0 and 20.0, so that the apparent abundance ($N(\text{Ca II})/N(\text{H I})$) decreases with increasing $N(\text{H I})$. As the datapoints in [Fig. 12-6](#) show, observationally the Ca II column density does indeed not vary much with $N(\text{H I})$ (as determined by Wakker and Mathis 2000). However, all the datapoints for Ca II lie below the colored model lines. In the case of the IVCs (open circles) the likely explanation is that calcium is heavily depleted onto dust grains, although this does not hide the trends in the Ca^+ ionization fraction. In the case of HVCs, the observed Ca II abundances lie below the model lines because the clouds have subsolar metallicity.

On average the following relation is found (see thick black line):

$$\begin{aligned}\log N(\text{Ca II}) &= 0.22 [\log N(\text{H I}) - 19.5] + 11.74 \\ \log A(\text{Ca II}) &= -0.78 [\log N(\text{H I}) - 19.5] - 7.76,\end{aligned}$$

(where $A(\text{Ca II})$ is defined as $N(\text{Ca II})/N(\text{H I})$).

This implies that on average the Ca II column density is $10^{11.8} \text{ cm}^{-2}$ for $N(\text{H I}) = 10^{20} \text{ cm}^{-2}$ and only decreases to $10^{11.4} \text{ cm}^{-2}$ when $N(\text{H I}) = 10^{18} \text{ cm}^{-2}$. Therefore, the Ca II H and K doublet provides a good way to determine cloud distances, as the lines will have similar strength in low and high column density gas. In addition, as the diagonal lines in [Fig. 12-6](#) show, the oscillator strength of the Ca II H and K doublet at 3934.777 and 3969.591 Å (vacuum wavelengths) is such that for gas with calcium abundance > 0.1 solar, the Ca II line is detectable in spectra with $S/N = 10$.

A final ion to discuss is Na I, as this has two strong absorption lines in the optical, at 5891.583 and 5897.558 Å. Na I is commonly detected in high column density low-velocity gas, and has been seen in a few IVCs, but not in HVCs. Its ionization balance is similar to that of Ca II, but the expected strengths of the absorption lines are such that in gas with low volume density the lines can only be detected in spectra with $S/N \sim 10$ if the gas-phase abundance of sodium is above ~ 0.25 solar, that is, the Na I doublet will generally not be detectable in clouds with subsolar metallicity and in clouds where a substantial fraction of the sodium is in dust grains.

3.5 Measured Distances and Metallicities

Wakker (2001) presented a comprehensive compilation of the published measurements of HVC absorption lines found in the spectra of stellar and extragalactic probes. That article also contains an extensive discussion of the distances and metallicities of individual HVC and IVC complexes, plus many maps and structural information. Since then, results from the *Far-Ultraviolet Spectroscopic Explorer (FUSE)* have provided much additional information concerning the metallicities of the HVCs. Many of those observations have been properly published (see Fox et al. 2004 and references therein), while others are only available in preliminary form

(as summarized by van Woerden and Wakker 2004). Further, *FUSE* detected H_2 in many IVCs, that is, in 50% of the directions where $\log N(\text{H I}; \text{IVC}) > 19.2$ (Wakker 2006). Finally, high-velocity O VI was found in >100 extragalactic sightlines (Sembach et al. 2003). To complement these UV results, observations with the Keck telescope, ESO's *Very Large Telescope (VLT)* and *Magellan* have yielded many additional distance brackets (Wakker et al. 2007; Wakker et al. 2008; Thom et al. 2006; Thom et al. 2008).

► **Table 12-2** summarizes available information on HVC distances and metallicities. Additional information for these clouds (such as mass and associated mass flows) can be found in Table 1 of Wakker (2004). ► **Figure 12-7** shows an example of stellar spectra that were used to derive a distance bracket to a cloud (core CIII in HVC complex C).

From ► **Table 12-2** it is clear that the distances to many of the larger HVC complexes (A, C, Anti-Center, GP) are on the order of 10 kpc, while the distances to the large IVCs (IV Arch, LLIV Arch, PP Arch) are only about 1 kpc. Some clouds appear to be more distant, however (clouds WW92, WW135, the Magellanic Stream). The cloud metallicities range from 0.09 times solar to about solar, with the values for complex C and the Magellanic Stream being the best determined. In some cases (complex A, complex WD), the derivation of a metallicity is complicated by the blending of O I $\lambda 1039.230 \text{ \AA}$ with lines of H_2 . It is clear, however, that the metallicity of the large IVCs is close to solar, while that of complex C is substantially subsolar, and that of the Magellanic Stream is similar to the value found in the Magellanic Clouds. Combined with the distances of ~ 1 kpc for the large IVCs, ~ 10 kpc for complex C, this is strong evidence for an explanation of the HVC phenomenon in which the large IVCs are related to the Galactic Fountain, complex C consists of low-metallicity accreting material, and the Magellanic Stream is a tidal stream pulled out of one or both of the Magellanic Clouds.

In the case of complex C an additional clue to its origin comes from the measurement of the deuterium to hydrogen ratio made by Sembach et al. (2004). They find $D/H = (2.2 \pm 0.7) \times 10^{-5}$. This value is (a) consistent with the primordial abundance of deuterium inferred from WMAP observations of the cosmic microwave background; (b) higher than that found for gas in the Galactic Disk, where deuterium is assumed to be destroyed inside stars, and (c) similar to values found in several QSO absorption line systems at redshifts >2 . Complex C is the *only* low-redshift cloud that has these three properties, and it thus provides an important anchor point for our understanding of the evolution of the D/H ratio.

4 Physical Properties of the HVCs

The internal structure of the HVCs gives important clues about their origin and fate. Relevant data include measurements of small-scale structure, velocity gradients, cloud size, temperature, density, pressure and timescales, ionization structure, and the relative amounts of neutral, ionized, and even molecular gas.

4.1 Small-Scale Structure

Maps of the HVCs have always shown structure down to the scale of the angular resolution. This is well illustrated by the case of complex A. With a $36'$ beam it appears to consist of several bright concentrations within a long filament (see ► **Fig. 12-1**). Observations with a $10'$ beam

■ Table 12-2

Known HVC distances and metallicities

HVC ^a	l, b_{cen}^b (deg)	v_{LSR}^c (km s ⁻¹)	Distance (kpc)	Dref	Metallicity (Z/Z _⊙)	Zref
Complex A (AIV)	155,38	-170:-140	>4.0	3		
Complex A (AVI)	160,45	-170:-140	2.0-10.0	9,29		
Complex C (CIA)	95,50	-150:-110	10.2-11.3	27	0.09	10,15,19,24,28
Complex C (CIIA)	130,54	-160:-140	7.4-10.9	23		
Complex C (CIIB)	115,54	-140:-110	<11.7	29	0.27	15,19
Complex C (CIIC)	120,58	-130:-110			0.15	14,19,20,24,28
Complex C (CD)	90,34	-190:-140	>12.6	27	0.19	18,24
Complex C (Cext)	65,38	-140:-120	<8.4	29		
Complex H	130,0	-220:-90	>5	6		
Mag. Stream		-430:+410	>30 ^d		0.25	7,11,12
ACII	195,-25	-150:-110	>2.7	25		
ACVHV (WW507)	168,-43	-350:-240	>0.3	16		
Cohen Stream (WW516)	145,-48	-170:-90	5.0-11.7	26		
Complex L	345,35	-190:-90	<4.5	29		
Complex GCP	40,-15	+90:+130	9.8-15.1	26		
Complex WA (WW135)	238,33	+100:+190	15-20	29		
Complex WB (WW92)	240,43	+90:+170	>20	29	0.2-0.6	21
Complex WD (WW226)	285,15	+110:+150			~0.1?	21
Complex WE	328,-15	+100:+120	<12.7	1		
Cloud WW35	249,52	+90:+120	6.4-8.3	22		
Complex M (MI)	165,65	-140:-110	3.4-4.3	29		
Complex M (MIII)	180,57	-120:-90	2.2-4.0	2,4,29		
Complex K	50,35	-100:-60	<6.8	16		
HVC100-7+110	100,-7	+100:+120	<1.3	8		
HVC224-83-197	224,-83	-190:-210			<0.5	17
IV Arch ^e	90,45	-95:-30	0.8-1.8	16	1.0	14
LLIV Arch ^e	150,32	-80:-30	0.9	16	1.0	13
Complex gp (g1)	67,-27	+55:+90	1.8-3.8	26		
Complex gp (g2)	35,-30	+55:+90	4.5	29		
PP Arch	120,-60	-80:-30	<0.9	16	~1.0	5

References: 1: Sembach et al. (1991); 2: Danly et al. (1993); 3: Wakker et al. (1996); 4: Ryans et al. (1997); 5: Fitzpatrick and Spitzer (1997); 6: Wakker et al. (1998); 7: Lu et al. (1998); 8: Stoppelenburg et al. (1998); 9: van Woerden et al. (1999a); 10: Wakker et al. (1999); 11: Gibson et al. (2000); 12: Sembach et al. (2001); 13: Richter et al. (2001a); 14: Richter et al. (2001b); 15: Gibson et al. (2001); 16: Wakker (2001); 17: Sembach et al. (2002); 18: Tripp et al. (2003); 19: Collins et al. (2003); 20: Sembach et al. (2004); 21: van Woerden and Wakker (2004); 22: Thom et al. (2006); 23: Wakker et al. (2007); 24: Collins et al. (2007); 25: Smoker et al. (2007); 26: Wakker et al. (2008); 27: Thom et al. (2008); 28: Shull et al. (2011); 29: Wakker et al. in preparation

^aCloud names WW # refer to the catalog of Wakker and van Woerden (1991)

^bApproximate Galactic longitude and latitude of center of complex

^cRange in LSR velocities

^dThe distance limit to the Magellanic Stream is based on numerical modeling

^eThe IV and LLIV Arch are the Intermediate-Velocity and Low-Latitude Intermediate-Velocity Arch, respectively

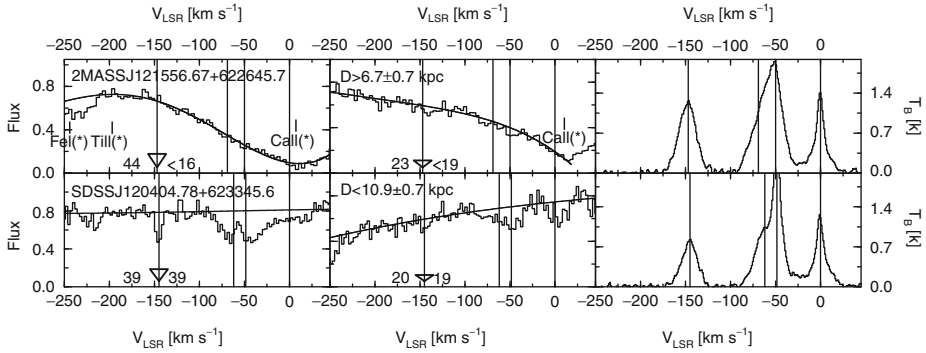


Fig. 12-7

Keck and LAB spectra for two stars that bracket the distance of core CIIIa in HVC complex C. Flux units are $10^{-16} \text{ erg cm}^{-2} \text{ s}^{-1} \text{ \AA}^{-1}$. *Left column*: Ca II K spectra (histograms) and continuum fits (*solid curves*); *middle column*: Ca II H spectra and continua (note that the left flux scale is valid only for Ca II K); *right column*: HI-21 cm spectra from the LAB survey. One star per row, with the name of the star and the implied lower or upper distance limit given in the top left corner of the K and H panels. Labels (Ca II(*), Fe I(*), and Ti II(*)) show the positions of stellar absorption lines. *Vertical lines* give the velocities of the H I components. *Triangles* and numbers near the bottom axes in each Ca II panel give the expected HVC absorption line, the expected equivalent width, and the 3σ detection limit or the detected equivalent width. For the star on the top the expected Ca II K equivalent width is 44 m\AA , whereas the 5σ detection limit is 16 m\AA , leading to a significant non-detection and a lower limit of $6.7 \pm 0.7 \text{ kpc}$ to the distance of the HVC, where the error in the derived star distance is 0.7 kpc . For the star on the bottom, the HVC's Ca II K line is detected with equivalent width 39 m\AA , while Ca II H is seen at the 19 m\AA level. This sets an upper limit of $10.9 \pm 0.7 \text{ kpc}$ to the cloud's distance

(Giovanelli et al. 1973; Brüns et al. 2001; Lockman et al. 2008) reveal smaller cores within the concentrations. Synthesis telescopes such as the Westerbork Synthesis Radio Telescope (*WSRT*) and the Australia Telescope Compact Array (*ATCA*) provide maps with about $1'$ resolution, showing even more details (Schwarz and Oort 1981; Wakker and Schwarz 1991; Wakker et al. 2002; de Heij et al. 2002a; Schwarz and Wakker 2004).

A noteworthy feature of the structure seen at the highest resolutions is that in general the details show no apparent relation to the HVC as a whole, and no clear signs of interaction with the local gas. Further, the small-scale structure has random velocities within the velocity width of the profile at lower resolution. This may indicate that the small-scale features are short-lived condensations within the HVCs (see also Sect. 4.2 on timescales below).

Several approaches have been used to numerically characterize the small-scale structure. Some of these just aim at deriving a number that can be compared between different clouds. Others are inspired by theoretical models of the ISM, especially the idea that the structure is generated by turbulence. In general, none of these methods has yet been applied to a large number of clouds, because they all require having a large dynamic range in resolution, whereas most observations only cover about one decade.

A different approach is to use the autocorrelation function (or its Fourier transform, the power spectrum), which contains information on the average two-dimensional spatial size,

orientation, and amplitude distribution of all features within the map. Usually just the (one-dimensional) azimuthal average of the power spectrum is used, and this often results in a power law. Although it is not the only possibility, the most likely process for generating a power law is turbulence. Turbulence generates fluctuations in both density and velocity, in a particular manner, namely, by having energy injected into the medium at a large scale, forming large eddies that break up into ever smaller eddies until the injected energy is thermalized. Lazarian and Pogosyan (2000) showed how it is possible to use 21-cm data to disentangle the velocity and density fluctuations by analyzing the power spectra in velocity slices of varying thickness. However, to apply their methods requires data with a large dynamic range in size scales, so that so far this method only remains a promising way to analyze the structure of the HVCs when better data becomes available. A simple method that shows promise for understanding whether turbulence is a likely origin of the small-scale structure in HI clouds is to look at density statistics, as discussed by Burkhart et al. (2009).

4.2 Timescales

Significant understanding of the properties of the HVCs is provided by the several timescales that can be deduced from the measured sizes and velocities. These timescales were discussed in detail by Wakker and van Woerden (1991, 1997). They include the ones summarized below. All these timescale estimates are proportional to the cloud's distance, D . Below, a value of $D = 10$ kpc was used to obtain the typical values.

4.2.1 The Time it Will Take for a Cloud to Reach the Galactic Plane

This is found as

$$t_{\text{fall}} = \frac{z}{v_z} = \frac{D \sin b}{\sqrt{2} v_{\text{DEV}} \sin b} = 69 \left(\frac{D}{10 \text{ kpc}} \right) \left(\frac{v_{\text{DEV}}}{100 \text{ km s}^{-1}} \right)^{-1} \text{ Myr},$$

where z is the cloud's height above the plane and v_{DEV} its deviation velocity. The factor $\sqrt{2}$ is valid when assuming that the cloud's velocity perpendicular to the line of sight has a magnitude similar to its radial velocity (after taking out the projection of the motion of the Sun). The downward acceleration by the Milky Way's gravity can be neglected, which might reduce the time by about 10 Myr.

4.2.2 The Time for the Cores to Shift Substantially Relative to Each Other

$$t_{\text{shift}} = \frac{s}{\sigma} = \frac{\alpha D}{\sigma} = 42 \left(\frac{D}{10 \text{ kpc}} \right) \left(\frac{\alpha}{5^\circ} \right) \left(\frac{\sigma}{20 \text{ km s}^{-1}} \right)^{-1} \text{ Myr},$$

where s is the linear separation between cores, α the angular separation of the cores, and σ the internal velocity dispersion between the motions of different parts of the cloud. This relation only makes sense for the larger complexes with multiple cores. The value of 20 km s^{-1} is the median dispersion for about 60 clouds with surface area larger than 15 square degrees.

4.2.3 The Time a Core takes to Move Across its Own Width

This is the ratio of the core radius to the deviation velocity:

$$t_{\text{core}} = \frac{R}{v_{\text{DEV}}} = \frac{\alpha D}{v_{\text{DEV}}} = 1.7 \left(\frac{D}{10 \text{ kpc}} \right) \left(\frac{\alpha}{1^\circ} \right) \left(\frac{v_{\text{DEV}}}{100 \text{ km s}^{-1}} \right)^{-1} \text{ Myr},$$

where R is the linear radius of the core and α its angular size, typically 1° .

4.2.4 The Time for a Core to Double its Size

If the expansion were unrestrained:

$$t_{\text{expand}} = \frac{R}{\Gamma} = \frac{\alpha D}{\Gamma} = 8.5 \left(\frac{D}{10 \text{ kpc}} \right) \left(\frac{\alpha}{1^\circ} \right) \left(\frac{\Gamma}{20 \text{ km s}^{-1}} \right)^{-1} \text{ Myr},$$

where again R is the linear radius of a core, while Γ is the velocity dispersion inside a core, for which the width of the 21-cm emission line is a good approximation.

Even with the uncertainties in the distances and the rough estimates of sizes, the derived timescales for the processes that determine the small-scale structure are clearly much shorter than the lifetime of a whole complex. Thus, the relative location and internal structure of the cloud cores (timescales (c) and (d)) will change considerably during the movement of a complex through space (timescale (a)), and our present view is only a snapshot of a dynamic process. On the other hand, the cores will more or less stay in the same configuration as the cloud falls, since timescales (a) and (b) are similar.

4.3 Ionization Structure and Volume Density

Having a measurement of both H I and H α emission, as well as a distance, allows a derivation of the volume density and of the ionization fraction in a cloud, with the only remaining uncertainty being the assumed internal geometry. Define s as the coordinate along the line of sight, $n(s)$ as the volume density structure, and $x(s)$ as the ratio of ionized to total hydrogen. Further write the electron density as $n_e = \epsilon n(\text{H}^+) = \epsilon x n$. Unless the gas is hot enough to contain substantial amounts of ionized helium (ionization potential 24.6 eV, corresponding to $\sim 20,000$ K), $\epsilon \sim 1$. If helium is fully ionized, $\epsilon = 1.2$. The “standard” model has constant density, a fully neutral core and fully ionized envelope, that is, $x = 0$ in the core and $x = 1$ outside it. Other simple possibilities are to assume a gaussian density profile, and/or constant ionization throughout. The volume density can be rewritten as $n(s) = n_o n'(s/L)$, where n_o is the central density and L a length parameter giving the diameter of the cloud. Observationally, one can measure the angular diameter of the cloud (α). When assuming that the thickness of the cloud is the same as its width, then $L = \alpha D$, with D the cloud’s distance.

The intensity of the H α recombination emission coming from the ionized gas is measured in terms of Rayleigh (R), with $1 \text{ R} = 10^6/4\pi \text{ photons cm}^{-2} \text{ s}^{-1} \text{ sr}^{-1}$ (see e.g., Haffner et al. 2003). But for a temperature-dependent factor, this is proportional to the emission measure (EM):

$$EM = \int n_e(s) n(\text{H}^+)(s) ds = 2.75 T_4^{0.924} I(\text{H}\alpha) \text{ cm}^{-6} \text{ pc},$$

where T_4 is the temperature T in units of 10^4 K. This temperature can be derived from observations of other optical emission lines, most notably [S II] $\lambda 6713$. In general, $T_4 \sim 1$.

With these definitions, the following relations hold:

$$\begin{aligned} N(\text{H}^+) &= \int x(s) n(s) ds = \mathcal{F}_1 n_o L \\ N(\text{HI}) &= \int (1 - x(s)) n(s) ds = (1 - \mathcal{F}_1) n_o L \\ EM &= \int \epsilon x^2(s) n^2(s) ds = \epsilon \mathcal{F}_2 n_o^2 L, \end{aligned}$$

where \mathcal{F}_1 and \mathcal{F}_2 are defined by these equations. Noting that $\epsilon \sim 1$, $T_4 \sim 1$, and $L = \alpha D$, and making a reasonable model for the density and ionization structure ($n(s)$ and $x(s)$) to give the structure factors \mathcal{F}_1 and \mathcal{F}_2 , these relations can be combined with the observables ($N(\text{HI})$, $I(\text{H}\alpha)$, α) to solve for the remaining two unknowns: n_o and $N(\text{H}^+)$. Observations of the forbidden [S II] emission line at 6713 \AA can be used to better constrain the temperature of the $\text{H}\alpha$ emitting gas (see Madsen et al. 2006 for a detailed description).

This method was applied to the H I, $\text{H}\alpha$ and S II absorption and emission data for HVC complex C in the sightline to Mrk 290 (Wakker et al. 1999). Inserting the recent measurement of the distance to this cloud (10 kpc) and assuming constant density and ionization fraction, this gives $n = 0.08 \pm 0.02 \text{ cm}^{-3}$, ionization fraction $x = N(\text{H}^+)/N(\text{H,tot}) = 17 \pm 10\%$, temperature $T = 7300 \pm 2000 \text{ K}$, and thermal pressure $P = 580 \pm 170 \text{ K cm}^{-3}$. Wakker et al. (2008) applied the same method to H I and $\text{H}\alpha$ for four clouds with known distance brackets, comparing the results using two different ionization models. In one model it is assumed that H^+ has the same pathlength as H I, in the other that $x = 0.5$ throughout. This resulted in volume densities in the range $0.05\text{--}0.15 \text{ cm}^{-3}$ and implied an ionized gas mass a factor 1–3 larger than the mass of neutral gas.

4.4 Molecules and Dust

Previous sections described the effects of dust on interpreting measurements of elemental abundances. The presence of and amount of dust in the clouds is also of intrinsic interest for two reasons: First, since dust usually forms due to stellar processes, the presence of dust in HVCs has implications for the history and origin of the gas. Second, through the well-established correlation between dust and molecules, dust gives information about the conditions in the cool cloud interiors. Direct searches for thermal dust emission from HVCs have been done using data from the Infra Red Astronomical Satellite (IRAS), with negative results for HVCs (Wakker and Boulanger 1986; Boulanger et al. 1996), but revealing emission from some IVCs (Désert et al. 1990; Weiss et al. 1999).

An indirect way to measure the presence of dust in HVCs is by comparing the abundances of heavy elements that are generally mostly in the gas phase (O, S) to those of elements that are generally present in the dust particles (e.g., Al, Fe, Ni). The analysis by Savage and Sembach (1996) shows that Si, Mg, Mn, Cr, Fe, and Ni are depleted by 0.3–0.8 dex in what they call “warm halo gas,” the measurements of which were done using several IVCs. Similar depletions were found in the LLIV Arch by Richter et al. (2001a). On the other hand, a detailed analysis of the relative abundances of different elements in complex C (Richter et al. 2001b) shows the absence of dust in this cloud, which suggests that it did not originate as gas in a stellar environment.

At the low densities typical for HVCs, molecular hydrogen (H_2) is only measurable by FUV absorption spectroscopy, requiring satellites in space, but then it can be seen at column densities as low as 10^{14} cm^{-2} . Using data from the FUSE satellite Wakker (2006) detects H_2 in 8 of 20 IVCs for which $\log N(\text{HI}) = 19.25\text{--}19.75$, and in 6 of 9 IVCs with $\log N(\text{HI}) > 19.75$, but in none of the IVCs for which $\log N(\text{HI}) < 19.25$. This is illustrated in [Fig. 12-8](#). Clearly, there is a transition from fully atomic gas to gas containing some H_2 at column densities above $2 \times 10^{19} \text{ cm}^{-2}$. On the other hand, the only H_2 at high velocity is seen in the Magellanic Stream, but not in 19 other sightlines, even though the median HI column density in these HVCs is $2 \times 10^{19} \text{ cm}^{-2}$.

No CO has been found in any HVC, even though deep searches were done toward selected dense cores (Wakker et al. 1997). In some IVC cores, however, CO has been detected. This includes the core IV21 in the IV Arch, toward which the intermediate-velocity HI is especially bright and narrow (Reach et al. 1994; Weiss et al. 1999), as well as several HI bright spots in the IV Spur (Magnani and Smith 2010). Since the CO emission is difficult to find and faint, no maps exist.

The hydrogen molecule is formed from neutral hydrogen when the volume density of the gas is sufficiently high (but only in the presence of a catalyst such as dust). H_2 is then destroyed by UV photons in the interstellar radiation field. Since this destruction takes away the photons, H_2 can survive in the denser central parts of a cloud. If there is an equilibrium between the formation and destruction of H_2 , then the following relation applies:

$$\frac{n(\text{HI})}{n(\text{H}_2)} = \frac{k\beta_0}{G T^{1/2} n(\text{H})},$$

where $n(\text{H}) = n(\text{HI}) + 2n(\text{H}_2)$ is the total volume density of protons. $k = 0.10 - 0.15$ is the probability that the molecule is dissociated after photon absorption, and β_0 is the photo-absorption rate per second. For a standard intensity of the interstellar radiation field

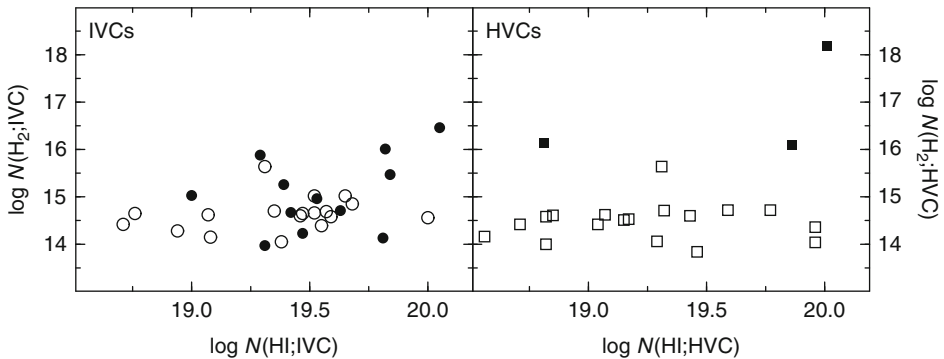


Fig. 12-8

Correlation between the column densities of atomic and molecular hydrogen in IVCs (*left*) and HVCs (*right*). Closed circles show detections, open circles are for upper limits. The detections of H_2 in HVCs are for a direction toward the Magellanic Stream (Fairall 9, Richter et al. 2001c), a direction toward the Leading Arm of the Stream (NGC 3783, Sembach et al. 2001), and a very small cloud at 75 km s^{-1} seen toward Mrk 153 (Wakker 2006). The 9 non-detections in HVCs with $\log N(\text{HI}) > 19.3$ include six sightlines through complex C, two through complex A, and one through the Outer Arm. The 13 detections in IVCs include 9 associated with the IV and LLIV Arch

($4\pi J_\lambda = 1.24 \times 10^{-5} \text{ W m}^{-2} \mu\text{m}^{-1}$; Mathis et al. 1983) $\beta_0 = 3.0 \times 10^{-10} \text{ s}^{-1}$. G is the probability per neutral H atom to form H_2 molecules by collisions with dust grains. In the Galactic Disk, $G = 9 \times 10^{-18} \text{ cm}^3 \text{ s}^{-1} \text{ K}^{-1/2}$ (van Dishoeck and Black 1986). This rate may differ in IVCs and especially in HVCs, however, as it depends on the presence of substantial amounts of dust, and because of the unknown surface properties of the dust grains in these clouds.

The problem with this equation is that it contains volume densities, while column densities are observed, and the H_2 will generally only be present in the regions with the highest densities. By defining χ as the strength of the interstellar UV radiation field relative to that near the Sun, and defining ψ as the fraction of the sightline where both H I and H_2 are present, the equilibrium relation can be turned into (Richter et al. 2003):

$$n_H \sim 1.2 \times 10^6 \frac{N(\text{H}_2)}{N(\text{H I})} \frac{\chi}{\psi} \text{ cm}^{-3}.$$

For the sightlines where intermediate-velocity H_2 is observed, the observed ratios of $N(\text{H}_2)/N(\text{H I})$ result in volume densities that range from $5/\psi$ to $35/\psi \text{ cm}^{-3}$, with a median of $27/\psi \text{ cm}^{-3}$. This implies pathlengths on the order of $\psi \text{ pc}$.

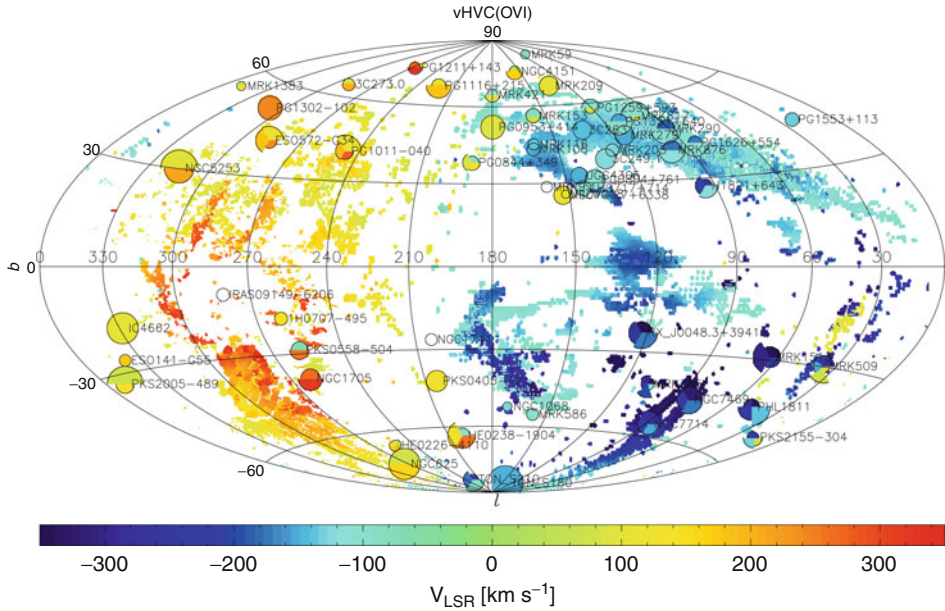
5 Hot Gas Associated with HVCs

In a 1956 paper, Spitzer pointed out that the lithium-like $(1s^2 2s)S_{1/2} \rightarrow (1s^2 2p)^2 P_{1/2,3/2}$ electronic transitions of O^{+5} , N^{+4} , C^{+3} , and Si^{+3} produce doublet absorption lines at wavelengths of 1031.9261/1037.6167 Å (O VI), 1238.821/1242.804 Å (N V), 1548.204/1550.781 Å (C IV), and 1393.7602/1402.7729 Å (Si IV). These ions have ionization potentials for production of 113.9, 77.5, 47.9, and 33.5 eV, which corresponds to temperatures in the range $1\text{--}3 \times 10^5 \text{ K}$. At these temperatures, interstellar gas is thermally unstable, as energy is carried off by photons emitted by collisionally excited ions, to which the medium is optically thin. At $T \sim 10^5 \text{ K}$ most of the energy loss is through resonance lines of oxygen (O IV, O V, O VI; see Sutherland and Dopita 1993). The presence of O VI, N V, C IV, and/or Si IV absorption therefore implies the existence of 10^6 K or hotter gas that has cooled down (or of a process that is heating up the gas).

The term “hot ISM” or “HIM” has often been used to describe gas with $T > 10^5 \text{ K}$, using “warm ISM” or “WIM” if the temperature is $\sim 5,000 \text{ K}$ to a few 10^4 K . However, since gas at temperatures $\sim 10^5 \text{ K}$ has very different properties than gas at $T > 5 \times 10^5 \text{ K}$ (not the least of which is that it cools relatively fast), Savage and Wakker (2009) proposed to instead use the term “transition temperature gas” for this quickly evolving phase, reserving “hot gas” for the X-ray emitting phase.

Starting in the 1970s, a sequence of spectroscopic facilities in space have observed the UV spectral lines of highly-ionized atoms. These include the Copernicus satellite, the International Ultraviolet Explorer (*IUE*), the Goddard High Resolution Spectrograph (*GHR*S), the Space Telescope Imaging Spectrograph (*STIS*), the Cosmic Origins Spectrograph (*COS*) (the latter three instruments on the Hubble Space Telescope), and the Far Ultraviolet Spectroscopic Explorer (*FUSE*). These instruments have found Si IV, C IV, N V, and O VI absorption in the Galactic Disk, with the most comprehensive studies those of Sembach and Savage (1992), Savage et al. (2001, 2003), Bowen et al. (2008), and Wakker et al. (2012).

Transition temperature gas at high velocity was first detected by Sembach et al. (1995, 1999) in the spectra of Mrk 509 and PKS 2155–304. The *FUSE* survey of O VI by Sembach et al. (2003) and the follow-up study of Fox et al. (2006) showed the ubiquity of this phase of the HVCs, as



■ Fig. 12-9

All-sky map showing the relation between the 21-cm HI high-velocity clouds (continuous background colors, cf. ● Fig. 12-1) and the high-velocity O VI absorption. A circle segment is shown for each sightline where high-velocity O VI is seen, with the color scale giving the velocities in the same manner as for the HI, and the radius of the segment proportional to the log of the O VI column density. Multiple circle segments in one direction indicate the presence of multiple absorption lines. Open circles are for directions without high-velocity O VI

high-velocity O VI was found in 85% of the 100 sightlines. ● Figure 12-9 compares the velocities of the O VI detections to the velocities of the 21-cm HVCs. With the possible exception of complex A, all 21-cm HVCs are found to have associated O VI absorption. High-velocity O VI is also seen away from the 21-cm clouds, with a large fraction of those cases occurring around the edges of large complexes such as complex C and the Magellanic Stream. Fox et al. (2006) found that in most of those cases (29 of 38, or 76%) there also is HI Lyman series absorption, with HI having column densities of 10^{15} – 10^{18} cm^{-2} . The average high-velocity O VI column density is $\log N(\text{O VI}) = 13.83$, and the distribution has a dispersion of 0.36 dex.

The presence of O VI in high-velocity clouds is most easily explained by concluding that they are embedded in a hot ($T > 5 \times 10^5$ K) surrounding medium. This is strongly supported by the fact that if both HI 21-cm emission and O VI absorption are seen, the velocities of these ions are well aligned (see Fox et al. 2004), but also by a comparison of predicted and observed column density ratios (see discussion below). That there is high-velocity O VI associated with the Magellanic Stream is therefore one of the strongest pieces of evidence for the existence of hot coronal gas around the Milky Way.

Several different mechanisms can produce highly-ionized gas in HVCs that are embedded in a hot corona. Numerical simulations give predictions for the column densities of the different

ions, as summarized below. Which processes are likely and unlikely can then be determined by comparing the predicted ionic ratios and column densities to the observed values.

For the following processes column density predictions have been published in the literature. These are compared with the observations in [Fig. 12-10](#). These models and their limitations are discussed in more detail by Wakker et al. (2012).

(1) *Collisional Ionization Equilibrium (CIE)*. In this case, at a fixed temperature every collisional ionization is balanced by a radiative recombination. Tables for the resulting ionic fractions were published by Sutherland and Dopita (1993) and by Gnat and Sternberg (2007). The predictions of these two papers are slightly different because of changes in atomic parameters (see references in Gnat and Sternberg 2007). Since many different processes affect the ISM (e.g., heating by supernovae, jostling by spiral arms and infall, cooling by photon emission), the gas is unlikely to be in CIE.

(2) *Shock ionization*. Shock fronts passing through the gas can create 10^5 K gas in which the highly-ionized atoms are present. Predictions for column densities were presented by Dopita and Sutherland (1996), for shock velocities of 200, 300, 400, and 500 km s⁻¹, magnetic parameter $B/n^{3/2} = 0, 1, 2$ and 4 $\mu\text{G cm}^{-3/2}$ (but only assuming solar abundances).

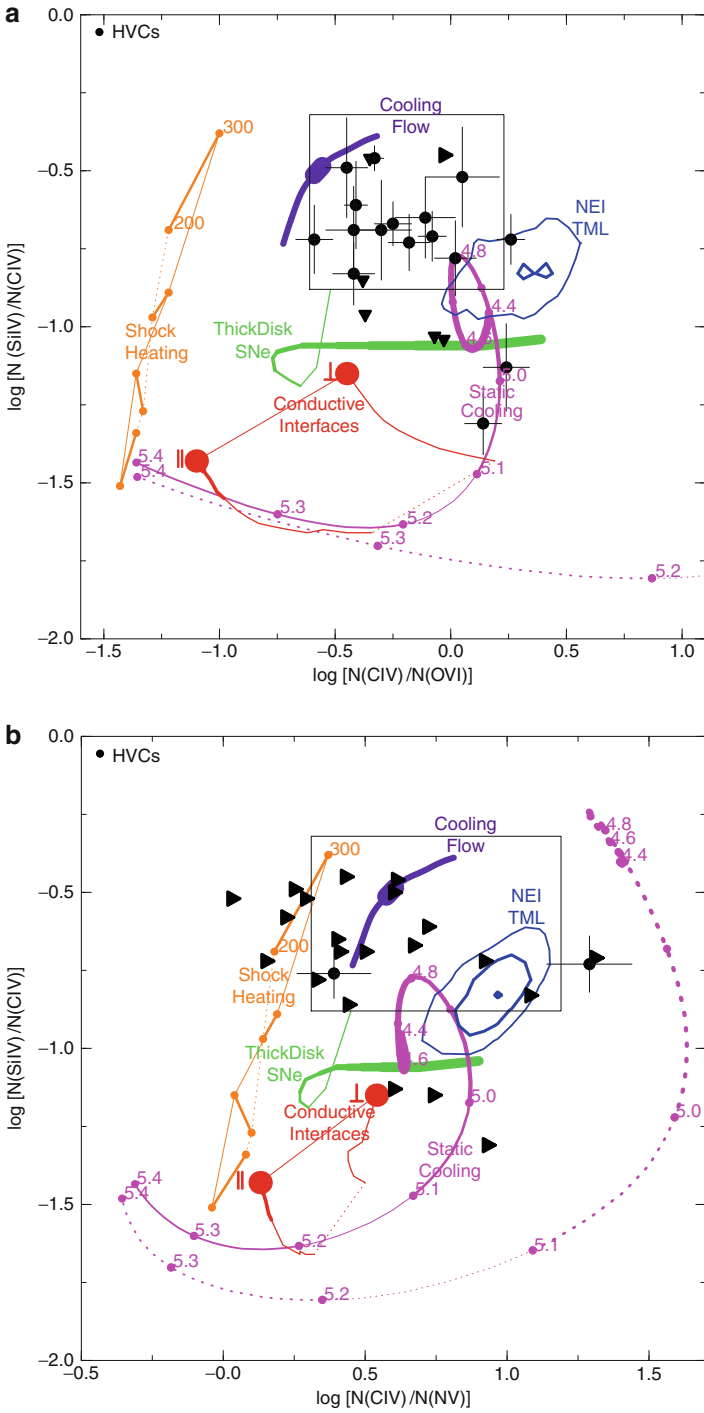
(3) *Static non-equilibrium radiative cooling*. In this kind of model a static parcel of gas starts out in CIE at a high temperature ($>5 \times 10^6$ K) and is allowed to cool, either isochorically (at constant density) or isobarically (at constant pressure). The resulting column densities were calculated by Gnat and Sternberg (2007). Most of the cooling is provided by metal-line emission, so the timescale is determined by the metallicity of the gas. At high metallicity the gas will cool faster than the highly-ionized atoms can recombine, leading to an overabundance of O VI, N V, and C IV relative to the amount present in CIE at the same gas temperature. Unlike what is the case for shock, conductive interface or turbulent mixing models, no absolute column densities are predicted by this model, only ratios.

(4) *Conductive interfaces*. If a region of cold (100 K) gas interfaces with a surrounding hot medium ($>5 \times 10^5$ K), electron thermal conduction transfers heat to the cold medium, creating gas at an intermediate temperature. After some time the heating will be balanced by radiative cooling, and a condensation front starts moving into the hot medium. Such interfaces were modeled in detail by Borkowski et al. (1990) and by Gnat et al. (2009). The models predict a thickness for the conductive interface on the order of 10 pc, with O VI and C IV column densities of about 5×10^{12} cm⁻².

(5) *Thick-Disk supernovae*. Shelton (1998) proposed that old supernovae that exploded in the Galactic Thick Disk (scaleheight 2 kpc) leave lingering amounts of highly-ionized gas that slowly recombines. She then predicted the time evolution of the column densities of the highly ionized atoms.

(6) *Turbulent Mixing Layers*. Gas at temperatures near 10^5 K can also be produced by turbulent mixing in shearing flows at the boundaries of hot and cold gas, as proposed by Begelman and Fabian (1990) and analyzed by Slavin et al. (1993), Esquivel et al. (2006), and Kwak and Shelton (2010). The latter of these presents a two-dimensional hydrodynamical calculation in which the non-equilibrium ionization of the different ions is followed. The earlier turbulent mixing models predict column densities in individual layers of $\sim 10^{12}$ cm⁻², much lower than what is observed, while the Kwak and Shelton (2010) models give $N \sim 10^{13}$ cm⁻². This implies that multiple interfaces are needed in a cloud to build up the observed median value of 7×10^{13} cm⁻².

(7) *Radiatively cooling gas flows*. If the cooling gas is moving, the thickness of the region where transition temperature gas is present will depend on the velocity of the flow. Detailed



■ Fig. 12-10
(continued)

models for this situation were summarized by Shapiro and Benjamin (1991), while more details can be found in the appendix included by Wakker et al. (2012). These authors also include photoionization due to photons generated in the hot phase, which is especially important for predicting the column density of Si IV.

Figure 12-10 compares the predictions to the observations for two pairs of ionic ratios, assuming that the gas has solar metallicity. In the panel on the top C IV/O VI is compared to Si IV/C IV, while the panel on the bottom gives the predictions for C IV/N V versus Si IV/C IV. Although these two ratios are similar, O VI is easier to detect than N V, and for many sight-lines high-velocity O VI has been measured. However, with existing missions only N V can be observed.

The predictions of the interface models (turbulent mixing, conductive interfaces, cooling flow) are expected to change if the gas has subsolar metallicity, as in that case cooling is less efficient. However, in models where the transition temperature gas is mostly formed by cooling (rather than by heating, as is the case for turbulent mixing), this should lead to a larger region where the cooling occurs. The increased pathlength then compensates for the lower efficiency, so that the resulting column densities of O VI, N V, and C IV should not be affected much. Unfortunately, except for the non-equilibrium cooling models of Gnat and Sternberg (2007) no detailed model calculations have been published for gas with subsolar metallicity, so this effect has not been directly confirmed.

Fig. 12-10

Theoretical ranges and observed values for three pairs of ionic ratios. DATA: Closed circles show ratios in individual HVC components; triangles show cases with one measured ratio and one upper limit. The square box encloses the range of observed ratios found in the Milky Way disk. MODELS: (1) Magenta lines (Static Cooling): non-equilibrium radiative cooling models from Gnat and Sternberg (2007), with $\log T$ labeled. The solid line is for solar metallicity gas, the dotted line for one tenth solar; the gas traverses this trajectory in about $3(0.001/n_0)$ Myr. In these models the gas is not flowing, and there is no additional heat input or output. (2) Orange lines (Shock Heating): Sutherland and Dopita (1993) shock models, with shock velocities of 200 and 300 km s^{-1} for the no-magnetic-field case marked and connected by a thick line. The other three thick line segments connect the 200 and 300 km s^{-1} case for higher magnetic parameters, $B n^{-3/2} = 1, 2,$ and $4 \mu\text{G cm}^{-3/2}$. (3) Red lines (Conductive Interfaces): conductive interface models from Borkowski et al. (1990), for perpendicular or parallel magnetic field (see the two symbols next to the red dots); the line thickness increases linearly with the age of the interface, 0.1 Myr at the thinnest point, 10 Myr at the other end, which is reached after 1–2 Myr. Thus, the line for this model appears as a quickly traversed thin red line ending in a large dot, after the ratios stabilize. (4) Green line (Thick Disk SNe): Shelton (1998) Thick Disk supernovae model, giving the evolution of the ratios with time (from 1 to 16 Myr after the supernova), with the line thickness proportional to the amount of time spent at each point. (5) Solid blue contours (NEI TML): distribution of ratios in the Kwak and Shelton (2010) turbulent mixing layer models, corresponding to 256 column densities derived by integrating through an interface at each 1 Myr long timestep between ages of 20 and 80 Myr. (6) Dark purple line (Cooling Flow): predictions of a model by Benjamin (see appendix in Wakker et al. 2012) for cooling hot gas flowing through an interface. The range of flow velocities is 14–16 km s^{-1} (thicker part of the line) and 9–26 km s^{-1} (thinner part)

Studies of the low-velocity absorption lines show that the absorption profiles of C IV and Si IV tend to be very similar, as are those of O VI and N V. Unfortunately, because of the lower cosmic abundance of nitrogen (as compared to oxygen or carbon), N V has so far been convincingly detected in only one HVC. Among the set O VI, N V, C IV, Si IV, the last two ions have the lowest ionization potential and photoionization may be important in their production. Except for the “Cooling Flow” model, this has not been taken into account in the predictions.

❖ *Figure 12-10* shows that *none* of the standard models of physical processes can reproduce *both* the observed C IV/O VI and the Si IV/C IV ratio in HVCs. The C IV/O VI ratio excludes shocks as a likely origin for the transition temperature gas. Conductive interfaces and halo supernovae seem incompatible with the Si IV/C IV ratio, although photoionization effects (not taken into account in the modeling) are expected to preferentially enhance Si IV, which may alleviate the discrepancy. Another problem with the conductive interface models is that they predict total column densities that are a factor 10–20 lower than what is observed. Static radiative cooling in gas with solar metallicity gives C IV/O VI and C IV/N V ratios that are similar to observations, but in low-metallicity gas straight cooling results in very different ratios than what is observed in HVCs. On the other hand, turbulent mixing and cooling flow models make predictions for Si IV/C IV, C IV/O VI/, and C IV/NV/ that are close to the observed range, although there are still some discrepancies. Further, in both of these types of models the total column density in a single layer is similar to the observed values (see discussion in Wakker et al. 2012).

With these caveats, it is clear that (a) the presence of transition temperature gas in HVCs implies that they are embedded in surrounding hot ($T > 5 \times 10^5$ K) gas, (b) the physical conditions in the interfaces are not fully understood, but they strongly indicate that non-equilibrium radiative cooling in a flow or mixing layer is likely to be important for creating the transition temperature gas seen in HVCs.

6 HVCs in and Around Other Galaxies

Since HVCs are observed from inside the disk of the Milky Way, only their radial velocities can be measured. Further, distances are known for only about 15 clouds. Thus, observations of HVCs in other galaxies may help our understanding. Various attempts have been made; for reviews see Oosterloo (2004), Sancisi et al. (2008), and Fraternali (2010).

Such observations have their own limitations, however. For distant galaxies the sensitivity and linear resolution are poor. For nearby galaxies, the nature of the data will depend on the galaxy’s inclination. Face-on galaxies allow direct measurements of the vertical component of cloud velocities, and they will show the horizontal shifts of clouds relative to features in the galactic disk. Edge-on galaxies directly provide the distance of clouds from the galactic plane, and show the horizontal component of the cloud velocities. For galaxies with intermediate inclinations, a more intricate analysis is required. Below, data on high-velocity gas for a few well-studied, nearby galaxies of various inclinations are discussed first. This is followed by a summary of the limited information available for a larger number of galaxies, and by some tentative conclusions.

6.1 A Face-on Galaxy: M 101

The large spiral galaxy Messier 101 is 5 Mpc distant and has low inclination, about 18° . Westerbork observations by van der Hulst and Sancisi (1988), with 0.6 kpc resolution, showed two

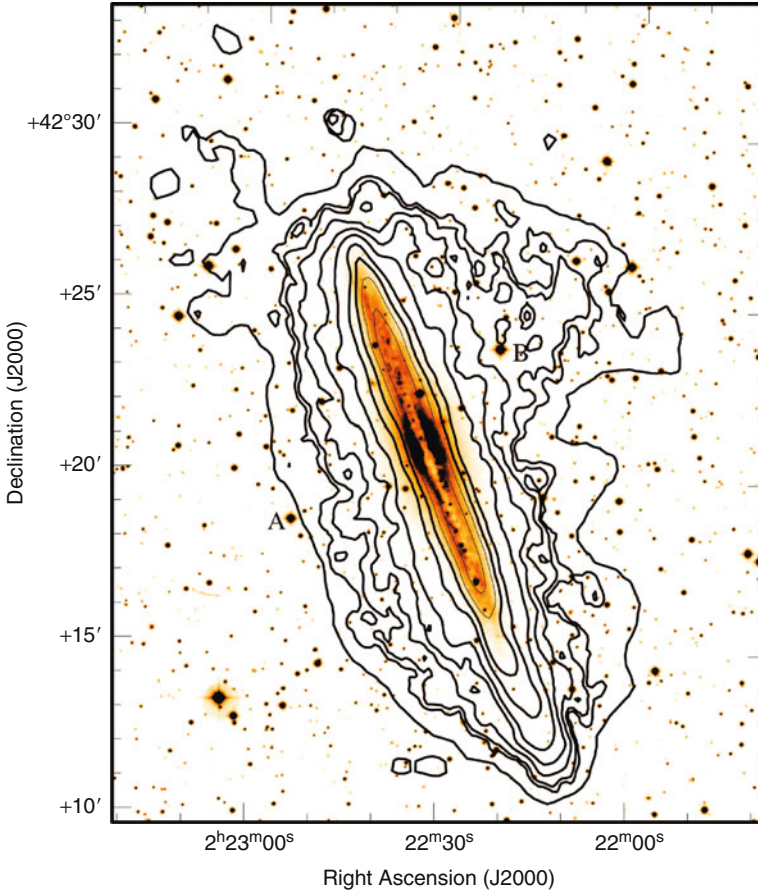
large HI clouds lying projected on M 101, with masses of 2×10^8 and $10^7 M_{\odot}$ and velocities of $+130$ and $+160 \text{ km s}^{-1}$ relative to the galaxy. Both clouds appear associated with a major hole in the galaxy's disk, evident also in position-velocity diagrams. The origin of the high-velocity clouds is not completely clear, but collisions of M 101 with large gas clouds are probable. A follow-up by Kamphuis et al. (1991) further describes an HI superbubble in M 101: a large (1.5 kpc diameter) hole in the disk, with gas moving away in two directions, at velocities of -50 and $+50 \text{ km s}^{-1}$. The shell has a mass of $3 \times 10^7 M_{\odot}$, and a kinetic energy exceeding 10^{53} erg, equivalent to 1,000 supernovae. This hole was first mentioned by Allen et al. (1973); it lies close to the H II complex NGC 5462, and may be related to it. The symmetry of motions suggests that the shell lies in the galactic plane, and is expanding into the halo.

6.2 An Edge-on Galaxy: NGC 891

This edge-on spiral galaxy lies at a distance of 9.5 Mpc, and has an inclination of at least 89° (Oosterloo et al. 2007). Early studies of H α spectra and images showed bubbles 0.5×1 kpc in size and diffuse H α emission up to $z = 2.4$ kpc (Pildis et al. 1994). Diffuse HI emission is found up to $z = 5$ kpc (Swaters et al. 1997). These studies also found that H α emission above the plane lags 40 km s^{-1} relative to the galaxy's rotation, while HI shows a lag of $25\text{--}100 \text{ km s}^{-1}$ (see also Heald et al. 2006a). Both the HI in the halo and the star formation in the disk were found to be stronger in the NE half of the galaxy. Deeper Westerbork observations by Oosterloo et al. (2007) (1.1×0.7 kpc resolution and HI detection limit $10^5 M_{\odot}$) show that the HI halo extends $10\text{--}15$ kpc from the plane, and locally even reaches $z = 22$ kpc (◆ Fig. 12-11). As much as 30% of the galaxy's HI lies in the halo. Oosterloo et al. (2007) also find halo clouds with mass $\sim 10^6 M_{\odot}$, some of which have "forbidden" (i.e., counter-rotating) velocities. Whether the halo HI is smoothly distributed or consists of clouds and complexes is not clear; this question requires higher resolution and sensitivity. Fitting 3-D models to Oosterloo's observations, Fraternali et al. (2005) find that purely ballistic fountain models fail, and that accretion of gas may be required. A 2-D rotation field shows a vertical rotation gradient of -15 km s^{-1} per kpc. Sancisi et al. (2008) note that these new observations have 50 times higher sensitivity than those of Sancisi and Allen (1979), but that the radial extent of the HI disk has not changed! Apparently, the HI halo extends only in the z -direction.

6.3 A High-Inclination Galaxy: NGC 2403

This nearby (3.2 Mpc), small spiral has an inclination of 63° . Following an initial analysis by Schaap et al. (2000), Fraternali et al. (2002a) analyzed VLA data with 0.2 kpc resolution (sensitive to clouds with $2 \times 10^4 M_{\odot}$) and found anomalous-velocity gas in position-velocity diagrams (the so-called *beard*; see ◆ Fig. 12-12). This is interpreted as originating from a 3 kpc thick HI component comprising $3 \times 10^8 M_{\odot}$ (10% of the galaxy's HI), that has a rotation lag of $25\text{--}50 \text{ km s}^{-1}$ in the inner parts, and an inward radial flow of 15 km s^{-1} . Long-slit spectra show that the ionized gas in the halo has the same rotation lag as the HI (Fraternali et al. 2004). Diffuse X-ray emission at 0.4–1 keV from the disk (described by Fraternali et al. 2002b) indicates a high star formation rate which probably is responsible for the disk/halo connection. All this fits with the results of Thilker et al. (1998) who identified 50 HI shells, determining their HI masses and kinetic energies. Combining all the evidence, the thick layer of HI and H α emission appears to be related to star formation in the disk through a Galactic Fountain.



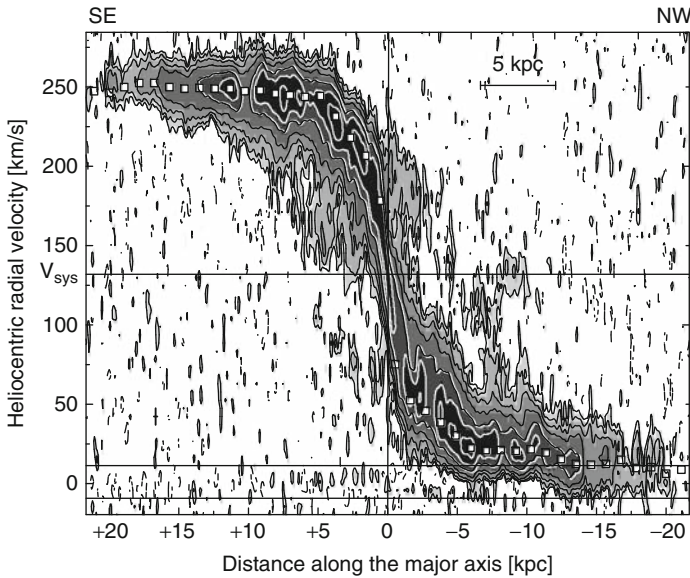
■ Fig. 12-11

Total H I image of NGC 891, obtained using the Westerbork Radio Telescope. The black contours are at 30'' resolution at levels of 0.1, 0.2, 0.5, 1, 2, 5, 10, 20, and $50 \times 10^{20} \text{ cm}^{-2}$. The outermost contour is at a resolution of 60'' and a level of $0.05 \times 10^{20} \text{ cm}^{-2}$ (From Oosterloo et al. 2007)

In addition to this evidence for a Fountain, the position-velocity diagrams also show a large (8 kpc) high-velocity cloud, and gas with “forbidden” velocities up to 130 km s^{-1} , both appearing to be signatures of accreting gas.

6.4 A Low-Inclination Galaxy: NGC 6946

This large spiral, at 6 Mpc distance, has an inclination of 38° . It was studied by Kamphuis and Sancisi (1993) and Boomsma et al. (2008), with the latter study having 400 pc resolution. There is widespread high-velocity H I in this galaxy, moving at up to 100 km s^{-1} relative to the underlying disk. Much of the anomalous-velocity gas is seen near holes in the H I distribution, 121 of which were listed by Boomsma et al. (2008) (mostly in the inner disk). As in other



■ Fig. 12-12

Position-velocity diagram ($1'$ wide slice) along the major axis of NGC 2403 ($15''$ spatial and 10.3 km s^{-1} velocity resolution). The central horizontal line shows the systemic velocity, the other two horizontal lines mark the channels contaminated by HI emission from the Milky Way. Contours are $-0.26, 0.26, 0.5, 1, 2, 5, 10,$ and 20 mJy beam^{-1} . White squares mark the rotation curves for the two sides of the galaxy. The “beard” of anomalous-velocity gas refers to the emission that lies between the rotation curve and the systemic velocity at distances ~ -10 to $+10$ arcmin along the major axis. Forbidden velocity gas can be seen at $(d, v) \sim (+3, +75)$ and $(d, v) \sim (-5, +175)$ (From Fraternali et al. 2002a)

galaxies, the extraplanar HI lags in its rotation by $50\text{--}100 \text{ km s}^{-1}$. The anomalous-velocity gas represents a total energy of 10^{55} erg, most of which is probably contributed by stellar winds and supernovae. However, Boomsma et al. (2008) also invoked accretion to explain several peculiar phenomena in the outer disk, including velocity anomalies, sharp edges, and a strong asymmetry outside the optical disk. While the extraplanar HI amounts to $3 \times 10^8 M_{\odot}$, or 4% of the total HI in this galaxy, and shows clumpy and filamentary structure, its z -distribution remains unknown because of the galaxy’s low inclination (Sancisi et al. 2008).

6.5 The Nearest Spiral Galaxies: Messier 31 and 33

At 0.77 and 0.8 Mpc distance, the Andromeda Galaxy (M 31) and the Triangulum Galaxy (M 33) are by far the nearest large spirals, and therefore of great potential interest for the study of HVCs. However, M 31 (with an inclination of 75°) is strongly warped (Brinks and Burton 1984); hence, distances of objects from the disk plane are difficult to assess. Two HI surveys with a 100-m class telescope have been published, having 2 kpc linear resolution and a detection limit of $\sim 10^5 M_{\odot}$. Thilker et al. (2004) used the Green Bank Telescope to cover a 94×94 kpc region,

while Westmeier et al. (2008) covered the galaxy out to a radius of 100 kpc with the Effelsberg telescope. These maps reveal discrete features up to 50 kpc away from the disk, with HI masses of 10^5 – $10^6 M_\odot$, and velocities comparable to those of outer-disk rotation. There also is a filamentary halo component of at least 30 kpc extent concentrated at the systemic velocity of M 31. Using Westerbork, Westmeier et al. (2005) mapped 9 HVC fields at resolutions of 0.11–0.45 kpc, and identified 16 of the Thilker et al. (2004) clouds as HVCs, with masses of order $10^5 M_\odot$ and sizes ~ 1 kpc; 12 of these lie in a 1-degree area, within 15 kpc of the disk. The latter HVC complex partly overlaps with the giant stellar stream discovered by Ibata et al. (2001), and has similar velocities, suggesting a possible tidal origin. However, other elongated systems of HI clouds show no relationships with the additional stellar streams discovered around M 31 by McConnachie et al. (2009). Westmeier et al. point out that the dark-matter satellites predicted by CDM scenarios (Klypin et al. 1999; Moore et al. 1999) are not seen. This may be explained if the clouds are predominantly ionized. Finally, the region around M 33 was mapped by Putman et al. (2009) with Arecibo (linear resolution 0.8 kpc, sensitivity limit $\sim 2 \times 10^4 M_\odot$). They found five clouds similar to the Galactic HVCs, with HI masses between 3 and $20 \times 10^4 M_\odot$. Their origins might lie in tidal disruption of M 33 by M 31, a few Gyr ago.

6.6 High-Velocity and Extraplanar Gas in Other Galaxies

In addition to the well-studied galaxies described above, evidence for anomalous-velocity gas is found in many other galaxies (see e.g., Fraternali 2010 for a tabulation). In a number of galaxies the thick disk has been seen in both HI and H α emission. This includes NGC 891 and NGC 2403, and also NGC 5775 (see Rand 2000 and Heald et al. 2006a). Lee et al. (2001) further found extraplanar molecular and X-ray emitting gas in NGC 5775. In most if not all of these cases, the rotation of the extraplanar gas appears to lag behind that of the main disk. Generally, these galaxies are actively forming stars, suggesting an origin of the extraplanar gas as the result of supernovae. However, UGC 7321 (Matthews and Wood 2003) presents a special case that may suggest additional processes can be important. Although it is a low-surface brightness galaxy, it has a halo of 3 kpc thickness; the energy source for this extraplanar gas can hardly be sought in supernovae.

Additional evidence for a relation between anomalous-velocity gas and star formation comes from the study of HI holes and shells. Following the discovery of a hole near NGC 5462 in M 101 (Allen et al. 1973), later described as a supershell by Kamphuis et al. (1991), holes and shells have been found in many galaxies. Brinks and Bajaja (1986) discussed HI holes in M 31 of sizes 100–1,000 pc, representing HI deficits of 10^3 – $10^7 M_\odot$ and energies of 10^{49} – 10^{53} erg; ages were estimated at 2–30 Myr. Similarly, Deul and den Hartog (1990) found more than 100 holes in M 33. In both cases, smaller high-contrast HI holes appeared to correlate with OB associations and giant H II regions, while large holes have H II regions and OB associations on their edges. Two HI supershells in NGC 4631 are even larger (2–3 kpc, masses $\sim 10^8 M_\odot$ and energies exceeding 10^{55} erg; Rand and van der Hulst 1993a; Rand and van der Hulst 1993b). In the case of NGC 6946, Boomsma et al. (2008) directly associated the many HI holes with anomalous-velocity gas. The data on HI holes and (super)shells argue strongly that groups of early-type stars in the disk, and the associated supernovae, are a feasible energy source for galactic fountains and hence for extraplanar gas.

6.7 Accretion of Gas by Galaxies

As discussed in more detail in [Sect. 7.3](#), there may be two modes of accretion: “hot accretion,” in which clouds condense out of a hot virialized halo (dominant around massive structures), and “cold accretion,” in which streams of cold gas find a way down (dominant in star-forming galaxies with lower halo masses). Cold accretion may involve merging with gas-rich satellites or infall from the intergalactic medium. Sancisi et al. (2008) reviewed the accumulating evidence for “cold accretion” by galaxies, considering four types of observational evidence:

- (1) Gas-rich dwarfs, or HI complexes, tails and filaments, indicative of “minor mergers” of a galaxy with a smaller one, or of recent arrival of external gas.
- (2) Extraplanar HI found in nearby galaxies, undoubtedly in large part produced by galactic fountains, but probably also partly of extragalactic origin.
- (3) Warped outer HI layers.
- (4) Lopsided disk morphology and kinematics.

Types 3 and 4 represent more tentative evidence than types 2 and, especially, 1. Sancisi et al. (2008) tabulate 23 galaxies with dwarf companions and/or peculiar HI structures, and discuss and illustrate many of these in detail. The HI masses involved range from 1 to $50 \times 10^8 M_{\odot}$. The optical morphologies vary from undisturbed to asymmetric and peculiar. The HI has advantages as an accretion indicator: it provides a direct measure of the accreting gas, and its distribution and kinematics lend themselves well to merger modeling.

How frequent are these accretion events? Two studies suggest that ~25% of galaxies show signs of present or recent tidal interactions: an HI survey of a magnitude- and volume-limited sample of galaxies in the Ursa Major Cluster by Verheijen and Sancisi (2001), and the Westerbork Survey of HI in Spiral and Irregular Galaxies (WHISP, 300 galaxies) by van der Hulst et al. (2001). However, the lifetimes of the HI features in question are only of order 1 Gyr; hence, the frequency of past accretion events may be much higher than 25%. The HI masses and lifetimes mentioned suggest accretion rates between 0.1 and $1 M_{\odot} \text{ yr}^{-1}$.

7 Origins of the High-Velocity Clouds

In the first 30 years after their discovery in 1963 by Muller et al., many different theories were proposed to explain the anomalous-velocity Galactic gas (see review by Wakker and van Woerden 1997). Some of these proposed origins can now be excluded, while others are supported by the data, which show that: (a) Many galaxies have a thick layer of extraplanar HI and other gas; this includes our own Milky Way, where individual HVCs are seen several kpc above the plane. (b) The kinematics of the Galactic HVCs and the HVCs seen around M 31 indicate the existence of a population of clouds extending several tens of kpc from the disk. (c) There is evidence for accretion of gas from dwarf galaxies and/or intergalactic clouds, both from the distribution of HI seen around other galaxies, the existence of the Magellanic Stream and the low metallicity of several Galactic HVCs. (d) The Galactic HVCs are embedded in a hot surrounding medium. With these observations, it now is clear that the HVC phenomenon includes a mix of populations with multiple origins. Since the HVCs are observationally defined in very general terms, this multiplicity of origins is not surprising. However, three processes in particular are

thought to be responsible for the high-velocity and intermediate-velocity gas, and these will be discussed below.

7.1 The Galactic Fountain

High-mass stars put a large amount of energy into the ISM via radiation, stellar winds, and supernovae. Cumulatively, they create superbubbles and eventually chimneys, which vent hot gas into the halo, resulting in an extended density-stratified (at least on average) atmosphere around the Galaxy. Radial and vertical pressure differences then set up flows. This model was first put forward by Shapiro and Field (1976), who considered the implications of the presence of a Galactic corona that produces the observed soft X-rays and O VI absorption. Bregman (1980) then showed how conservation of angular momentum leads to an outward motion of the upwelling gas, and to an inward motion of the return flow. He proposed that this process can produce the HVCs. However, after further study (e.g., Mac Low et al. 1989; Houck and Bregman 1990; Rosen and Bregman 1995; de Avillez and Breitschwerdt 2005) it has become clear that the resulting apparent velocities are more similar to those seen for the IVCs. Bregman (2004) presents an extensive discussion of all the theoretical and observational aspects of the Galactic Fountain.

The temperature of the Galactic coronal gas is estimated to be $\sim 5 \times 10^5$ K by combining inferences from X-ray emission (see McCammon and Sanders 1990 and Snowden et al. 1998), the presence of transition temperature gas with a scaleheight of a few kpc (Savage and Wakker 2009), and CIV and O VI emission lines (Martin and Bowyer 1990; Shelton et al. 2007). The density of the 5×10^5 K gas in the disk, n_0 , can be estimated in the manner presented by Benjamin (2004), who shows the densities for an isothermal 10^6 K halo using the galactic potential model of Dehnen and Binney (1998). A more direct observational estimate comes from comparing X-ray and O VIII line absorption and emission (Bregman and Lloyd-Davies 2007). Both of these methods suggest that $n_0 \sim 10^{-3}$ near the Sun.

Assuming that there is a source of hot gas, the argument of Kahn (1976, 1981) reveals the physical conditions under which a fountain flow will develop. First define the mean atomic mass number $m_a = \sum_{\text{elements}} A_{\text{el}} m_{\text{el}} \sim 1.23 m_H$, with A_{el} and m_{el} the abundance by number and the atomic mass of each element, and m_H the mass of a hydrogen atom (1.67×10^{-27} kg; $A(\text{H}) = 0.925$ and $A(\text{He}) = 0.074$). Second, define the mean particle mass, m_p , which includes counting the electrons. In fully ionized gas ($T > 10^5$ K) $m_p \sim 0.5 m_a$. m_a is used to calculate the mass density $\rho = m_a n_H$, while m_p is used to calculate the pressure, $P = \frac{\rho}{m_p} kT$. Finally, near the Sun, the gravity above the stellar layer is $g_z = 6.25 \times 10^{-9}$ cm s $^{-2}$ (Kuijken and Gilmore 1991).

Given these definitions, the sound speed c_s is given by:

$$c_s = \left(\frac{\gamma P}{\rho} \right)^{1/2} = \left(\frac{\gamma k}{m_p} \right)^{1/2} T^{1/2} \sim 67 \left(\frac{T}{10^{5.3}} \right)^{1/2} \text{ km s}^{-1}$$

where $\gamma = 5/3$ is the ratio of specific heats. Thus, the natural scaleheight of the hot ISM is $H = c_s^2/g_z \sim 2.3(T/10^{5.3})$ kpc. The dynamical timescale for the gas flow is given by:

$$t_{\text{dyn}} = \frac{c_s}{g_z} \sim 34 \left(\frac{T}{10^{5.3}} \right)^{1/2} \left(\frac{6.25 \times 10^{-9}}{g_z} \right)^{-1} \text{ Myr.}$$

Kahn (1976) showed how to estimate the cooling timescale, by calculating the rate of energy loss per unit mass (Q) and comparing this to the rate of change of specific entropy (s): $Ds/Dt = Q/T$. This is done by approximating the standard interstellar cooling function (Λ in units of $\text{erg cm}^3 \text{ s}^{-1}$) at temperatures above 10^5 K by a power law. Then:

$$Q = \frac{\Lambda n_H}{m_a} \text{ erg s}^{-1} \text{ g}^{-1} \text{ with}$$

$$\Lambda = 1.33 \times 10^{-19} T^{-1/2} \text{ erg cm}^3 \text{ s}^{-1}.$$

Given a volume V and a number of particles N , the entropy of a monatomic ideal gas is:

$$S = Nk \log \left[\frac{V}{N} \left(\frac{U}{N} \right)^{3/2} \right] + \text{Constant}.$$

Inserting $U = (3/2)NkT$ for the internal energy, using $M = Nm_p$, and defining $\kappa = P\rho^{-5/3}$, the specific entropy ($s = S/M$) can then be written as:

$$s = \frac{k}{m_p} \log \left(\kappa^{3/2} \right) + \text{Constant}.$$

Using κ , and using that $Ds/Dt = Q/T$, it can be shown that:

$$\frac{D\kappa^{3/2}}{Dt} = \frac{-1.33 \times 10^{-19} k^{1/2}}{m_a^2 m_p^{1/2}} = -q,$$

with $q \sim 3.6 \times 10^{32} \text{ cm}^6 \text{ g}^{-1} \text{ s}^{-4}$. Since q is a constant, this gives the cooling time due to radiative losses as:

$$t_{\text{cool}} = \frac{\kappa^{3/2}}{q} = \frac{P^{3/2}}{q\rho^{5/2}} = \frac{k^{3/2}}{q m_p^{3/2} m_a} \frac{T^{3/2}}{n_H} = 5.8 \left(\frac{T}{10^{5.3}} \right)^{3/2} \left(\frac{10^{-3}}{n_H} \right) \text{ Myr}.$$

The ratio of the cooling timescale to the dynamical timescale is therefore:

$$\frac{t_{\text{cool}}}{t_{\text{dyn}}} = \gamma^{-1/2} \frac{P}{\rho^2} \frac{g_z}{q} \sim 0.17 \left(\frac{T}{10^{5.3}} \right) \left(\frac{10^{-3}}{n} \right).$$

Thus, near the Sun, the cooling time is much shorter than the dynamical time. Therefore, if there is a source of hot gas, it will cool before it reaches hydrostatic pressure equilibrium (with a scaleheight of about 2–3 kpc). The cool gas will lose buoyancy and rain down to the plane. Since the gravity, density, and temperature of the hot gas vary considerably across the Galaxy, a Fountain flow may not be present everywhere, however. Near the Galactic Center, the situation changes since the gravitational potential is no longer plane-parallel and the gas temperature is higher. Then a Galactic Wind may occur (e.g., Breitschwerdt et al. 1993; Everett et al. 2008).

The identification of at least some IVCs (specifically the IV Arch and LLIV Arch) with the return flow of a Fountain is based on their near-solar metallicity (showing they originated in the disk), the fact that their dust content is lower than that of gas in the disk (suggesting the dust was partially destroyed when the gas was ejected from the disk), their height above the plane ($\sim 0\text{--}2 \text{ kpc}$) and their velocities (about 50 km s^{-1} downward motion). There is also evidence for mostly ionized gas at $z \sim 1 \text{ kpc}$ that is flowing up (cloud g1, Wakker et al. 2008). However, for many other IVCs the metallicity and distance have not yet been measured, so it remains unclear whether these would also represent Fountain clouds.

To derive the mass flow rate corresponding to these clouds requires an estimate of their vertical velocity, which is not directly observed, but which can be estimated. A reasonable first guess can be made by using v_{DEV} , assuming that the tangential component of the velocity vector is equal to the radial component, and projecting v_{DEV} . Then, summing the column density ($N(\text{HI})$) over each telescope beam (with size $d\Omega$) that covers the cloud:

$$\dot{M} = \frac{Mv_z}{z} = \int \sqrt{2} v_{\text{DEV}} \sin b m_{\text{H}} N(\text{HI}) D d\Omega,$$

where m_{H} is the mass of an H atom and D the cloud distance. Using the parameters for the IV and LLIV Arches ($v_{\text{DEV}} = 50 \text{ km s}^{-1}$, $b = 45^\circ$, $N(\text{HI}) = 10^{20} \text{ cm}^{-2}$, $\Omega = 5,000$ square degrees, $D = 1 \text{ kpc}$) shows they represent a circulation rate of $\sim 0.06 M_{\odot} \text{ yr}^{-1}$ within 1 kpc of the Sun. Assuming that the Fountain covers $\sim 25\%$ of the Galaxy (300 kpc^2 out to $R = 10 \text{ kpc}$), the total circulation rate would be about $4.5 M_{\odot} \text{ yr}^{-1}$.

A completely independent way of estimating the mass flow rate comes from the intensity of the C IV emission line, which is proportional to the product of the density of the ionized gas (n , in cm^{-3}) and the velocity of the flow (v , in km s^{-1}). Observations (Martin and Bowyer 1990) imply $n v = 1.8 \times 10^5 \text{ cm}^{-2} \text{ s}^{-1}$. Theoretically, the circulation rate is simply given by the equation of mass conservation. Translating to quantities useful for Galactic studies, the two-sided mass flow rate is


$$\dot{M} = 4.3 \left(\frac{f}{0.25} \right) \left(\frac{nv}{1.8 \times 10^5 \text{ cm}^{-2} \text{ s}^{-1}} \right) \left(\frac{R}{10 \text{ kpc}} \right)^2 M_{\odot} \text{ yr}^{-1}.$$

Here R is the radius of the area of the disk where a Fountain occurs, while f is the fraction of the disk covered by the flow. Although based on only a few datapoints, this shows that the flow rate obtained from UV line emission and from the observed IVCs is of the same order of magnitude, giving confidence in the Fountain picture and its associated numbers. However, in order to firm up these estimates, more and better distances are needed for IVCs, as are more observations of C IV (and O VI) emission.

7.2 Tidal Streams

The Magellanic Stream has long been identified as gas pulled out from the Small Magellanic Cloud (SMC), either by tidal forces or by ram-pressure stripping. Such an origin is strongly supported by measurements of the metallicity of $Z/Z_{\odot} \sim 0.3$ found for gas in both the leading and trailing parts of the Stream (Lu et al. 1998, Wakker et al. 2002, using NGC 3783, and Gibson et al. 2000, using Fairall 9). The implied presence of dust in the Stream also supports this idea (Richter et al. 2001c). Such a metallicity is consistent with the abundances for stars and gas in the LMC and SMC.

In theoretical models of tidal stripping (Gardiner and Noguchi 1996; Mastrogiuseppe et al. 2005; Connors et al. 2006), the combined tidal force of the Milky Way and the LMC extracted the outer gaseous parts of the SMC during the previous perigalactic passage of the Magellanic Clouds, 1.5 Gyr ago. Affected by hydrodynamical interactions with the Milky Way's gaseous corona, decelerated and accelerated gas then formed a long stream, predicted to have distances of 50–100 kpc. During the most recent perigalacticon (~ 0.2 Gyr ago) more gas was extracted, resulting in the “Magellanic Bridge,” gas now located between the Clouds. This model is supported by the fair match between the observed and predicted locations and velocities of the

Stream, especially the so-called “Leading Arm.” Note that Putman et al. (1998) use this term for the short and small structure centered on $l = 320^\circ$, $b = -22^\circ$ (see  Fig. 12-1). However, the main body of the Leading Arm extends to $l = 265^\circ - 290^\circ$, $b = +30^\circ$.

It is also possible that some of the gas in the Stream originated from ram pressure stripping, as the Magellanic Clouds move through the hot coronal medium surrounding the Milky Way. As discussed by Bregman (2004) and Bregman and Lloyd-Davies (2007), near the LMC the density of the coronal gas is at most about 10^{-4} cm^{-3} . Moving through this with a velocity of $\sim 300 \text{ km s}^{-1}$, the gas in the Clouds sees a ram pressure that is comparable to the gravitational force (see e.g., Moore and Davis 1994). Thus, gas in the LMC is safe, but gas in the outer parts of the SMC might be stripped. In the case of even smaller dwarf galaxies passing within 200 kpc from the Milky Way, this seems to have been the case, since none of the nearby dwarfs has much remaining gas (Grcevich and Putman 2009).

However, estimates of the proper motion of the MCs (Kallivayalil et al. 2006) and new cloud orbits (Besla et al. 2007) have thrown a wrench into this picture. These results would suggest much larger distances for the Stream ($\sim 150 \text{ kpc}$). In this case the Stream would consist of gas pulled out of the SMC by the LMC without the help of the Milky Way. A model calculation that predicts the distribution of Stream gas was made by Besla et al. (2010). It does a fair job of predicting the location and velocities of the main body of the Stream, as do the older tidal models. However, in this situation it is more difficult to form a Leading Arm that extends north of the Galactic plane. Besla et al. (2010) predict a modest amount of gas $10^\circ - 20^\circ$ ahead of the LMC. The tidal models in which the Stream has orbited the Milky Way more than once predict a Leading Arm that is much longer, which is required to explain the presence of gas with Magellanic metallicity seen toward NGC 3783, 50° from the LMC.

The Magellanic Stream is probably only the most well-defined and prominent example of the removal of gas from dwarf galaxies that orbit the Milky Way. Many other high-velocity clouds may have originated in this manner. However, in no other case has it been possible to make the link between a HVC and an identified existing or past dwarf. In the case of the cloud that has been named HVC 40–15+100, complex GCP, complex GP or “the Smith Cloud” by different authors, Lockman et al. (2008) model its orbit by assuming that the elongated appearance is due to tidal stretching, and interpreting the observed velocity gradient as a projection effect. Similarly, the elongated appearance of complexes A and C suggests that tidal stretching plays a role. However, there has not been a study that deduces the associated orbit, and no stellar counterparts have been identified for any of these HVCs.

One possible problem with identifying HVCs as tidal debris is that after the stripping takes place, the gas is no longer gravitationally bound and thus it will expand unless it is confined by hot coronal gas. However, in that case it will heat up and may evaporate, also disappearing from view in 21-cm observations.

7.3 Low-Metallicity Accretion

One of the most important processes traced by HVCs is the accretion of low-metallicity ($Z/Z_\odot \sim 0.1$) material onto the Galaxy, which dilutes the metals formed by stars. Such accretion is the theorists’ favorite method to solve the “G-dwarf problem” (see e.g., Pagel 1997), the

fact that the metallicity distribution of G-dwarfs (long-lived stars that have continually been born since the formation of the Milky Way disk) is narrower than that predicted by closed-box models. The theoretically favored models imply a present-day infall rate of about $0.4 M_{\odot} \text{ yr}^{-1}$ (Chiappini 2008).

Some of the HVCs provide evidence that such accretion is indeed ongoing. The metallicity of the second-largest HVC (complex C) has been measured as $Z/Z_{\odot} \sim 0.15$ (Wakker et al. 1999; Fox et al. 2004 and references therein). Furthermore, it has an (N/O) ratio that is about one fifth solar (this number includes ionization corrections). Thus, complex C consists of gas that has never been part of the Galaxy, but is about to accrete. Its distance is ~ 10 kpc (Wakker et al. 2007). Combined with its estimated vertical velocity ($50\text{--}150 \text{ km s}^{-1}$, depending on the location in the cloud) and total gas mass ($\sim 10^7 M_{\odot}$ in hydrogen and helium and, assuming a 50% hydrogen ionization fraction), this implies a mass accretion rate of $0.1\text{--}0.25 M_{\odot} \text{ yr}^{-1}$ in complex C alone. A number of other HVCs are also suspected of having a metallicity of $\sim 1/10$ th solar (e.g., complex A and the Anti-Center HVCs), although more evidence is needed. Tentative distance brackets on the order of 10 kpc exist for some of these clouds. If these metallicities and distances can be confirmed, they would combine to an additional mass accretion rate of about $0.05\text{--}0.1 M_{\odot} \text{ yr}^{-1}$. Further accounting for clouds in the population that are hidden by low-velocity gas (see [Sect. 2.5](#)), these rates suggest that the total accretion rate (summing both the neutral and the ionized phase) represented by low-metallicity HVCs is similar to the predicted amount.

The ultimate origin of this infalling gas is still unclear, however. An unknown fraction (possibly all) of the accreting gas may originally have been part of old tidal streams, similar to the Magellanic Stream. The Stream itself is a likely source of about $10^8 M_{\odot}$ of $Z/Z_{\odot} = 0.25$ gas over the next few Gyr. As long as the accreting gas has a metallicity on the order of 0.1 times solar, it makes little difference for the chemical evolution models whether the accreting gas originates in a tidal stream or is more pristine. However, the amount of gas available from the known population of dwarf galaxies near the Milky Way (and near M 31) is several orders of magnitude below the required infall rate (Grcevich and Putman 2009), so that a fully tidal origin seems unlikely. Thus, a different mechanism is needed. Three mechanisms have been proposed (see Dekel and Birnboim 2006), which lead to subtly different predictions for the behavior of the HVC population.

7.3.1 Fragmentation in a Hot Halo

The first mechanism for the origin of HVCs is that they are the observable result of the fragmentation of a hot corona as it cools. This kind of model was originally proposed by Oort (1970), who suggested that it might take a long time before all the gas in the Milky Way's gravitational sphere of influence would make it to the disk. In a more hydrodynamically oriented version of this idea (White and Rees 1978), intergalactic gas that falls into dark matter potential wells heats to the virial temperature ($T = 10^6 (v_{\text{max}}/163)^2 \text{ K}$), and the denser gas at small radii then cools and accretes. This reduces the pressure support of the more distant gas, which falls in, gets denser, and cools in turn. Following ideas of Mo and Miralda-Escude (1996), Maller and Bullock (2004) use this picture, but work out the consequences of dropping the assumption that the cooling is uniform. Instead they assume that clouds form by fragmentation, and then derive the typical parameters of such clouds. Using the same notation as in [Sect. 7.1](#), the energy loss per unit mass is again given by $Q = \Lambda n_H / m_a$, but now Q is given by $(3/2 k T_h) / (m_p t_f)$, with t_f

the time since the halo formed. This gives a characteristic “cooling density,” ρ_c , the mass density above which the gas can cool after time t_f :

$$\rho_c = \frac{3 m_a^2 k T_h}{2 m_p^2 t_f \Lambda(T, Z)},$$

where T_h is the temperature of the hot halo gas. Note that here it is assumed that $\Lambda(T, Z)$ is proportional to the metallicity, Z , of the gas. For a halo in which gas has a metallicity $Z = 0.1$ solar, and taking $t_f = 8$ Gyr, the number density n_H then is $\sim 1.5 \times 10^{-4} \text{ cm}^{-3}$. Now, when a mostly neutral cloud forms (having temperature $T_w \sim 10^4$ K, and density ρ_w), it will end up in pressure equilibrium with the hot gas. Defining the average halo pressure as \bar{P}_h , then $P_w = \bar{P}_h$ for the typical cloud that forms. Maller and Bullock (2004) show that $\bar{P}_h \sim 2.7 P_c = \eta_P P_c$, with P_c the pressure corresponding to ρ_c . This implies $\rho_w = \rho_c (\eta_P T_h / T_w)$, so that:

$$r_{cl} = \left(\frac{3 M_{cl}}{4\pi \rho_w} \right)^{1/3} \sim 1050 \left(\frac{M}{5 \times 10^6 M_\odot} \right)^{1/3} \left(\frac{T_h}{10^6 \text{ K}} \right)^{-1/2} \left(\frac{T_w 10^6}{10^3 T_h} \Lambda_Z \frac{t_f}{10^8 \text{ Gyr}} \right)^{1/3} \text{ pc},$$

where r_{cl} is the cloud’s radius, M is the cloud mass, $\Lambda_Z = \Lambda(10^6, Z) / \Lambda(T, Z)$ is the value of the cooling function relative to that at $T = 10^6$ K, and metallicity $Z = 0.1$ solar. The only thing left to determine is the typical cloud mass. Maller and Bullock (2004) present arguments based on the limits set by different physical processes (evaporation, conduction, thermal instabilities, drag, self-gravity) and conclude that for a Milky Way–sized halo, $M_{cl} \sim 5 \times 10^6 M_\odot$. The infall of these clouds is then driven by drag and cloud–cloud collisions, from which they derive the typical infall time and thus the growth rate of a galaxy.

This approach predicts the presence of clouds with typical diameter about $2.4 (D/50 \text{ kpc})$, and (assuming 50% ionization) a typical HI column density $4 \times 10^{19} \text{ cm}^{-2}$, which is just a little bit larger and brighter than the typical properties of the observed population of small HVCs. However, the model also predicts a total mass in cold clouds of about $2 \times 10^{10} M_\odot$, which would imply the presence of 4,000 HVC-like clouds in the halo. This is an order of magnitude larger than the number that is observed. Reconciling this with the observed population might be done by assuming a much smaller neutral fraction ($<5\%$), making the implied HI column density smaller, so that most clouds would go undetected in 21-cm HI emission.

7.3.2 Cold, Filamentary Streams

Kereš and Hernquist (2009) used simulations to confirm an alternative way to produce cool clouds embedded in hot coronal gas as a natural consequence of structure and galaxy formation in the universe. Their model consists of a cosmological simulation of structure formation caused by dark matter in a $10h^{-1} \text{ Mpc}$ box. At $z = 99$ they populate a Milky Way–sized box ($200h^{-1} \text{ kpc}$ on the side) with gas particles. Following the hydrodynamic and thermodynamic state of this gas (including heating, average cooling, and a simple prescription for ionization by UV photons, but excluding outflows from the galaxies in the box), they then find that some cool neutral clouds that lose angular momentum and accrete are formed in the “hot mode” manner described above. However, some of the gas never gets hotter than 10^5 K before it reaches the galaxy disk. Furthermore, this gas streams in mostly along the large-scale filaments created by the dark matter, causing an asymmetric inflow, unlike what is the case for the hot-mode accretion. According to Kereš et al. (2009), for dark matter halos below $5 \times 10^{10} M_\odot$ all accretion

follows the cold-mode route, while in dark matter halos above $3 \times 10^{11} M_{\odot}$ (galaxy mass above $3 \times 10^{10} M_{\odot}$) hot mode accretion is more important.

The model predicts the existence of 100–1,000 clouds with $T < 30,000$ K and $n > 0.004 \text{ cm}^{-3}$ at distances up to about 50 kpc, with masses of 10^6 to a few $10^7 M_{\odot}$ (although the lower limit is probably due to the resolution of the simulation), accreting at a rate of $\sim 1 M_{\odot} \text{ yr}^{-1}$. At $z \sim 0$ about 10% of the gaseous halo mass is in the cold phase, which is in a dynamical equilibrium between cloud formation, destruction, and accretion. Clearly, the properties of this cloud population are similar to those of the observed HVCs, except for the density, which is observed to be on the order of 0.1 cm^{-3} for the larger clouds about 10 kpc from the plane, although estimates suggest a value more like 0.01 cm^{-3} for small (likely to be more distant) clouds. Further, in this model the infalling clouds have no metals.

Clearly, current understanding of the formation of clouds in a hot corona that surrounds galaxies predicts that HVC-like objects can form and accrete. What is not clear yet is which of the two modes is most compatible with the detailed characteristics of the HVCs, that is, their distribution with longitude and latitude, their velocities, their metallicities, their internal structure, density, etc. Furthermore, the physical processes used in the models are either only approximated analytically, or follow simple prescriptions for the microphysics to predict the conditions in $10^6 M_{\odot}$ gas “particles,” while the effects of UV radiation and feedback flows are only partially dealt with. Finally, in these models the state of the gas is not followed at temperatures below 10^4 K.

7.3.3 Sweeping up of Coronal Gas by Fountain Flows

In a series of papers, Fraternali and collaborators have considered the effects of the interaction of Fountain clouds with hot coronal gas. Fraternali and Binney (2006) pointed out that a continuous-outflow model of Fountain clouds can reproduce the z -distribution of extraplanar H I that is observed in the nearby spirals NGC 891 and NGC 2403 (see Sects. 6.2 and 6.3). However, this model fails to reproduce the observed vertical gradient in the rotation velocity and it also predicts a radial outflow rather than the observed radial inflow.

Fraternali and Binney (2008), Marinacci et al. (2010), and Marasco et al. (2011) show that these kinematic failures can be resolved if Fountain clouds sweep up and cause cooling in hot coronal gas. The amount of gas stripped from a Fountain cloud might be similar to the amount of cooled coronal gas condensed in the cloud’s wake. The result would be a disk accretion rate, valid also for the Milky Way Galaxy, of about two solar masses per year, with half of that fresh low-metallicity gas.

This model also can be fit to the LAB data for the Milky Way. Marasco and Fraternali (2011) find that the data can be reproduced using a model with a scale height of halo H I (1.6 kpc), a vertical rotation gradient of $15 \text{ km s}^{-1} \text{ kpc}^{-1}$ and a radial inflow of 30 km s^{-1} .

7.4 Summary of Origins

High-velocity clouds (broadly defined) appear to have multiple origins.

- (1) Some clouds with velocities that deviate by up to about 80 km s^{-1} from differential galactic rotation have metallicities that are near solar (the IV Arch, the LLIV Arch,

and the PP Arch) and distances on the order of 1 kpc or less. Some clouds are moving away from the disk at $50\text{--}80\text{ km s}^{-1}$ (cloud g1) and have similar amounts of ionized and neutral hydrogen. These clouds fit the predicted properties of a Galactic Fountain return flow and outflow. From their masses, distances, and velocities it is possible to derive the circulation rate of gas between the Milky Way disk and halo. Preliminary estimates give values on the order of $4.5 M_{\odot} \text{ yr}^{-1}$. This implies that all of the ISM ($\sim 5 \times 10^9 M_{\odot}$) circulates through the lower halo on timescales of a Gyr.

- (2) Other HVCs clearly are connected to the Magellanic Clouds, in particular the Magellanic Stream, which originates from the Clouds. The Stream gas has metallicities similar to those in the SMC. It most likely has a tidal origin, although ram pressure effects may have contributed to its formation, and certainly they are contributing to its current location and velocities. A number of HVCs are not in the main body of the Stream, but based on their location, velocities, internal properties, and metallicities they appear related to the processes that formed the Stream; this is especially true for the clouds with velocities $>200\text{ km s}^{-1}$ in the region $l = 260^{\circ}\text{--}300^{\circ}$, $b = -20^{\circ}$ to $+30^{\circ}$. The discovery of O VI absorption associated with the Stream shows that it is embedded in hot ($>10^6\text{ K}$) coronal gas. Note that this implied corona has a different origin than the lower-temperature corona that is formed at heights a few kpc above the Galactic disk by the escape of hot gas from superbubbles and supernovae.
- (3) The properties of the two large complexes in the northern sky (complex A and C) suggest that they represent the last stages of the infall of low-metallicity material from intergalactic space – they are elongated, suggesting tidal stretching, and in the case of complex C the measured metallicity is ~ 0.15 times solar, the D/H ratio is high, and the N/O ratio is subsolar. Other clouds, such as many (or all) of the ones in the Anti-Center region, may also fit into this category. The total infall rate of baryons associated with these objects is on the order of $0.2\text{--}0.4 M_{\odot} \text{ yr}^{-1}$ (assuming equal amounts of neutral and ionized gas in these clouds).
- (4) Finally, there are many smaller HVCs, which have a size spectrum that is a power law, and whose velocities and distribution on the sky can be understood in a model in which they have distances up to 80 kpc and they mostly orbit the Milky Way, but with random velocities that have a dispersion of 50 km s^{-1} and a net infall velocity of 50 km s^{-1} for the population. For some of these clouds distances of 10–20 kpc have been found. Models of structure formation in the universe predict similar populations of clouds, but do not yet correctly predict the detailed cloud properties.

The challenges for the future include the following: (a) Determining for each HVC into which of these possible origins it fits, so that a proper determination of the circulation and accretion rates becomes possible. (b) Comparing the observations of the locations and velocities of the HVCs with the predictions for the formation of Galactic Fountain clouds, the Magellanic Stream and condensations in hot coronas. (c) Comparing the observed physical conditions (density, temperature, pressure, ionization fraction, interface properties) of the clouds with the predictions of the different models. (d) Finding HVC analogs around external galaxies, to allow generalizing the understanding of such objects and determining correlations with galaxy properties.

Cross-References

- ▶ [Astrophysics of Galactic Charged Cosmic Rays](#)
- ▶ [Dark Matter in the Galactic Dwarf Spheroidal Satellites](#)
- ▶ [Dynamics of Disks and Warps](#)
- ▶ [Galactic Distance Scales](#)
- ▶ [Gamma-Ray Emission of Supernova Remnants and the Origin of Galactic Cosmic Rays](#)
- ▶ [History of Dark Matter in Galaxies](#)
- ▶ [Magnetic Fields in Galaxies](#)
- ▶ [Mass Distribution and Rotation Curve in the Galaxy](#)

References

- Adams, W. S. 1949, *ApJ*, 109, 354
- Allen, R. J., Goss, W. M., & van Woerden, H. 1973, *A&A*, 29, 447
- Arnal, E. M., Bajaja, E., Larrarte, J. J., Morras, R., & Pöppel, W. G. L. 2000, *A&AS*, 142, 35
- Asplund, M., Grevesse, N., Sauval, A. J., & Scott, P. 2009, *ARA&A*, 47, 481
- Bajaja, E., Cappa de Nicolau, C. E., Cersosimo, J. C., Martin, M. C., Loiseau, N., Morras, R., Olano, C. A., & Pöppel, W. G. L. 1985, *ApJS*, 58, 143
- Barger, K. A., Haffner, L. M., Hill, A. S., Wakker, B. P., Madsen, G. J., & Duncan, A. K. 2012, *ApJ* (submitted)
- Beers, T. C., Wilhelm, R., Doinidis, S. P., & Mattson, C. J. 1996, *ApJS*, 103, 433
- Begelman, M. C., & Fabian, A. C. 1990, *MNRAS*, 244, 26
- Benjamin, R. A. 2004, in *High-Velocity Clouds, Astrophysics and Space Science Library*, Vol. 312 (Dordrecht: Kluwer), 371
- Benjamin, R. A., & Danly, L. 1997, *ApJ*, 481, 764
- Bertoldi, F., & McKee, C. F. 1992, *ApJ*, 395, 140
- Besla, G., Kallivayalil, N., Hernquist, L., Robertson, B., Cox, T. J., van der Marel, R. P., & Alcock, C. 2007, *ApJ*, 668, 949
- Besla, G., Kallivayalil, N., Hernquist, L., van der Marel, R. P., Cox, T. J., & Kerés, D. 2010, *ApJ*, 721, L97
- Bland-Hawthorn, J., & Maloney, P. R. 1999, *ApJ*, 510, L33 (erratum 2001, *ApJ*, 553, L231)
- Bland-Hawthorn, J., Veilleux, S., Cecil, G. N., Putman, M. E., Gibson, B. K., & Maloney, P. R. 1998, *MNRAS*, 299, 611
- Blitz, L., Spergel, D., Teuben, P., Hartmann, D., & Burton, W. B. 1999, *ApJ*, 514, 818
- Boomsma, R., Oosterloo, T. A., Fraternali, F., van der Hulst, J. M., & Sancisi, R. 2008, *A&A*, 490, 555
- Borkowski, K. J., Balbus, S. A., & Frstrom, C. C. 1990, *ApJ*, 355, 501
- Boulanger, F., Abergel, A., Bernard, J. P., Burton, W. B., Désert, F.-X., Hartmann, D., Lagache, G., & Puget, J.-L. 1996, *A&A*, 312, 256
- Bowen, D. V., Jenkins, E. B., Tripp, T. M., Sembach, K. R., Savage, B. D., Moos, H. W., Oegerle, W. R., Friedman, S. D., Gry, C., Kruk, J. W., Murphy, E., Sankrit, R., Shull, J. M., Sonneborn, G., & York, D. G. 2008, *ApJS*, 176, 59
- Braun, R., & Burton, W. B. 1999, *A&A*, 341, 437
- Braun, R., & Thilker, D. A. 2004, *A&A*, 417, 421
- Breitschwerdt, D., McKenzie, J. F., & Völk, H. J. 1993, *A&A*, 269, 54
- Bregman, J. N. 1980, *ApJ*, 236, 577
- Bregman, J. N. 2004, in *High-Velocity Clouds, Astrophysics and Space Science Library*, Vol. 312, (Dordrecht: Kluwer), 341
- Bregman, J. N., & Lloyd-Davies, E. J. 2007, *ApJ*, 669, 990
- Brinks, E., & Bajaja, E. 1986, *A&A*, 169, 14
- Brinks, E., & Burton, W. B. 1984, *A&A*, 141, 195
- Brown, W. R., Geller, J. M., Kenyon, S. J., Beers, T. C., Kurtz, M. J., & Roll, J. B. 2004, *AJ*, 127, 1555
- Brüns, C., Kerp, J., & Pagels, A. 2001, *A&A*, 370, L26
- Burkhart, B., Falceta-Gonçalves, D., Kowal, G., & Lazarian, A. 2009, *ApJ*, 693, 250
- Chiappini, C. 2008, *ASP Conf Ser*, 396, 113
- Collins, J. A., Shull, J. M., & Giroux, M. L. 2003, *ApJ*, 585, 336
- Collins, J. A., Shull, J. M., & Giroux, M. L. 2007, *ApJ*, 657, 271
- Connors, T. W., Kawata, D., & Gibson, B. K. 2006, *MNRAS*, 371, 108
- Cutri, R. M., et al. 2003, 2MASS All Sky Catalog of Point Sources (VizieR Online Data Catalog #2246)
- Danly, L., Albert, C. E., & Kuntz, K. D. 1993, *ApJ*, 416, L29

- Davies, R. D., Buhl, D., & Jafolla, J. 1976, *A&AS*, 23, 181
- de Avillez, M. A., & Breitschwerdt, D. 2005, *A&A*, 436, 585
- de Heij, V., Braun, R., & Burton, W. B. 2002a, *A&A*, 391, 67
- de Heij, V., Braun, R., & Burton, W. B. 2002b, *A&A*, 392, 417
- Dehnen, W., & Binney, J. 1998, *MNRAS*, 294, 429
- Dekel, A., & Birnboim, Y. 2006, *MNRAS*, 368, 2
- Désert, F.-X., Bazell, D., & Blitz, L. 1990, *ApJ*, 355, L51
- Deul, E. R., & den Hartog, R. H. 1990, *A&A*, 229, 362
- Dopita, M. A., & Sutherland, R. S. 1996, *ApJS*, 102, 161
- Espreate, J., Cantó, J., & Franco, J. 2002, *ApJ*, 575, 194
- Esquivel, A., Benjamin, R. A., Lazarian, A., Cho, J., & Leitner, S. N. 2006, *ApJ*, 648, 1043
- Everett, J. E., Zweibel, E. G., Benjamin, R. A., McCammon, D., Rocks, L., & Gallagher, J. S. 2008, *ApJ*, 674, 258
- Ferland, G. 1996, Hazy, a brief introduction to CLOUDY, Univ. Kentucky Ph. Dept. Report
- Ferrara, A., & Field, G. B. 1994, *ApJ*, 423, 665
- Fitzpatrick, E. L., & Spitzer, L. 1997, *ApJ*, 475, 623
- Fox, A. J., Savage, B. D., Wakker, B. P., Richter, P., Sembach, K. R., & Tripp, T. M. 2004, *ApJ*, 602, 738
- Fox, A. J., Savage, B. D., & Wakker, B. P. 2006, *ApJS*, 165, 229
- Fraternali, F. 2010, *AIP Conf*, 1240, 135
- Fraternali, F., & Binney, J. 2006, *MNRAS*, 366, 449
- Fraternali, F., & Binney, J. 2008, 386, 935
- Fraternali, F., van Moorsel, G., Sancisi, R., & Oosterloo, T. A. 2002a, *AJ*, 123, 3124
- Fraternali, F., Cappi, M., Sancisi, R., & Oosterloo, T. A. 2002b, *ApJ*, 578, 109
- Fraternali, F., Oosterloo, T. A., & Sancisi, R. 2004, *A&A*, 424, 485
- Fraternali, F., Oosterloo, T. A., Sancisi, R., & Swaters, R. A. 2005, *ASP Conf*, 331, 239
- Fujimoto, M., & Sofue, Y. 1976, *A&A*, 47, 263
- Gardiner, L. T., & Noguchi, M. 1996, *MNRAS*, 278, 191
- Gibson, B. K., Giroux, M. L., Penton, S. V., Putman, M. E., Stocke, J. T., & Shull, J. M. 2000, *AJ*, 120, 1830
- Gibson, B. K., Giroux, M. L., Penton, S. V., Stocke, J. T., Shull, J. M., & Tumlinson, J. 2001, *AJ*, 122, 3280
- Giovanelli, R. 1980, *AJ*, 85, 1155
- Giovanelli, R., & Haynes, M. P. 1977, *A&A*, 54, 909
- Giovanelli, R., Verschuur, G. L., & Cram, T. R. 1973, *A&AS*, 12, 209
- Girardi, L., Bertelli, G., Bressan, A., Chiosi, C., Groenewegen, M. A. T., Marigo, P., Salasnich, B., & Weiss, A. 2002, *A&A*, 391, 195
- Gnat, O., & Sternberg, A. 2007, *ApJS*, 168, 213
- Gnat, O., Sternberg, A., & McKee, C. F. 2009, *ApJ*, 718, 1315
- Grcevich, J., & Putman, M. E. 2009, *ApJ*, 696, 385
- Green, R. F., Schmidt, M., & Liebert, J. 1986, *ApJS*, 61, 305
- Haffner, L. M. 2005, in *ASP Conf. Proc.*, *Extraplanar Gas*, Vol. 331, ed. R. Braun, 25, Kluwer
- Haffner, L. M., Reynolds, R. J., & Tufte, S. L. 2001, *ApJ*, 556, L33
- Haffner, L. M., Reynolds, R. J., Tufte, S. L., Madsen, G. J., Jaehnig, K. P., & Percival, J. W. 2003, *ApJS*, 149, 405
- Hartmann, D., & Burton, W. B. 1997, *Atlas of Galactic Neutral Hydrogen* (Cambridge: Cambridge University Press)
- Heald, G. H., Rand, R. J., Benjamin, R. A., Collins, J. A., & Bland-Hawthorn, J. 2006a, *ApJ*, 636, 181
- Heald, G. H., Rand, R. J., Benjamin, R. A., & Bershad, M. A. 2006b, *ApJ*, 647, 1018
- Hill, A. S., Haffner, L. M., & Reynolds, R. J. 2009, *ApJ*, 703, 1832
- Houck, J. C., & Bregman, J. N. 1990, *ApJ*, 352, 506
- Hulsbosch, A. N. M. 1975, *A&A*, 40, 1
- Hulsbosch, A. N. M., & Wakker, B. P. 1988, *A&AS*, 75, 191
- Ibata, R., Irwin, M., Lewis, G., Ferguson, A. N. M., & Tanvir, N. 2001, *Nature*, 412, 49
- Ivezić, Ž., Vivas, A. K., Lupton, R. H., & Zinn, R. 2005, *AJ*, 129, 1096
- Kahn, F. D. 1976, *A&A*, 50, 145
- Kahn, F. D. 1981, in *Investigating the Universe: Papers presented to Zdenek Kopal on the Occasion of his Retirement, September 1981* (Dordrecht: Reidel), 1
- Kalberla, P. M. W., Burton, W. B., Hartmann, D., Arnal, E. M., Bajaja, E., Morras, R., & Pöppel, W. G. L. 2005, *A&A*, 440, 775
- Kalberla, P. M. W., McClure-Griffiths, N. M., Pisano, D. J., Calabretta, M. R., Ford, H. A., Lockman, F. J., Staveley-Smith, L., Kerp, J., Winkel, B., Murphy, T., & Newton-McGee, K. 2010, *A&A*, 521, A17
- Kallivayalil, N., van der Marel, R. P., & Alcock, C. 2006, *ApJ*, 652, 1213
- Kamphuis, J. J., Sancisi, R., & van der Hulst, J. M. 1991, *A&A*, 244, L29
- Kamphuis, J. J., & Sancisi, R. 1993, *A&A*, 273, L31
- Kereš, D., & Hernquist, L. 2009, *ApJ*, 700, L1
- Kereš, D., Katz, N., Fardal, M., Davé, R., & Weinberg, D. H. 2009, *MNRAS*, 395, 160

- Klypin, A., Kravtsov, A. V., Valenzuela, O., & Prada, F. 1999, *ApJ*, 522, 82
- Kravtsov, A., *AdAstr* 2010, E8, *Advances in Astronomy*, Volume 2010, Article ID 281913
- Kuijken, K., & Gilmore, G. 1991, *ApJ*, 367, L9
- Kukarkin, B. V., et al. 1970, *General Catalogue of Variable Stars*, Vols. I and II (3rd ed.; Moscow: Sternberg Institute)
- Kuntz, K. D., & Danly, L. 1996, *ApJ*, 457, 703
- Kwak, K., & Shelton, R. L. 2010, *ApJ*, 719, 523
- Lazarian, A., & Pogosyan, D. 2000, *ApJ*, 537, 720
- Lee, S. W., Irwin, J. A., Dettmar, R. J., Cunningham, C. T., Golla, G., & Wang, Q. D. 2001, *A&A*, 377, 759
- Lehner, N., & Howk, J. C. 2011, *Science*, 334, 955
- Lin, D. N. C., & Lynden-Bell, D. 1982, *MNRAS*, 198, 707
- Lockman, F. J. 2003, *ApJ*, 591, L33
- Lockman, F. J., Benjamin, R. A., Heroux, A. J., & Langston, G. I. 2008, *ApJ*, 679, L21
- Lu, L., Savage, B. D., Sembach, K. R., Wakker, B. P., Sargent, W. L. W., & Oosterloo, T. A. 1998, *AJ*, 115, 162
- Mac Low, M.-M., McCray, R., & Norman, M. L. 1989, *ApJ*, 337, 141
- Madsen, G. J., Reynolds, R. J., & Haffner, L. M. 2006, *ApJ*, 652, 401
- Magnani, L., & Smith, A. J. 2010, *ApJ*, 722, 1685
- Maller, A. H., & Bullock, J. S. 2004, *MNRAS*, 355, 694
- Maloney, P. 1993, *ApJ*, 414, 41
- Maloney, P. R., & Putman, M. E. 2003, *ApJ*, 589, 270
- Marasco, A., & Fraternali, F. 2011, *A & A*, 525, A134
- Marasco, A., Fraternali, F., & Binney, J. 2011, *MNRAS*, 419, 1107
- Marinacci, F., Binney, J., Fraternali, F., Nipoti, C., Ciotti, L., & Londrill, P. 2010, *MNRAS*, 404, 1464
- Martin, C., & Bowyer, S. 1990, *ApJ*, 350, 242
- Mastropietro, C., Moore, B., Mayer, L., Wadsley, J., & Stadel, J. 2005, *MNRAS*, 363, 509
- Mathis, J. S., Mezger, P. G., & Panagia, N. 1983, *A&A*, 128, 212
- Matthews, L. D., & Wood, K. 2003, *ApJ*, 593, 721
- McCammon, D., & Sanders, W. T. 1990, *ARA&A*, 28, 657
- McConnachie, A. W. et al. 2009, *Nature*, 461, 66
- Mo, H. J., & Miralda-Escude, J. 1996, *ApJ*, 469, 589
- Moore, B., & Davis, M. 1994, *MNRAS*, 270, 209
- Moore, B., Ghigna, S., Governato, F., Lake, G., Quinn, T., Stadel, J., & Tozzi, P. 1999, *ApJ*, 524, L19
- Morras, R., Bajaja, E., Arnal, E. M., & Pöppel, W. G. L. 2000, *A&AS*, 142, 25
- Morton, D. C. 2003, *ApJS*, 149, 205
- Muller, C. A., Oort, J. H., & Raimond, E. 1963, *C R Acad Sci Paris*, 257, 1661
- Münch, G. 1952, *PASP*, 64, 312
- Murphy, E. M., Lockman, F. J., & Savage, B. D. 1995, *ApJ*, 447, 642
- Oort, J. H. 1966, *BAN*, 18, 421
- Oort, J. H. 1970, *A&A*, 7, 381
- Oosterloo, T. A. 2004, in *High-Velocity Clouds*, ASSL, 312, 125
- Oosterloo, T. A., Fraternali, F., & Sancisi, R. 2007, *AJ*, 134, 1019
- Osterbrock, D. E. 1989, *Astrophysics of Gaseous Nebulae and Active Galactic Nuclei* (Mill Valley: University Science Books)
- Pagel, B. 1997, *Nucleosynthesis and Chemical Evolution of Galaxies* (Cambridge: Cambridge University Press)
- Peek, J. E. G., Heiles, C., Douglas, K. A., Lee, M.-Y., Grcevich, J., Stanimirovic, S., Putman, M. E., Korpela, E. J., Gibson, S. J., Begum, A., Saul, D., Tobishaw, T., & Krco, M. 2011, *ApJS*, 194, 20
- Pildis, R. A., Bregman, J. N., & Schombert, J. M. 1994, *ApJ*, 423, 190
- Pisano, D. J., Barnes, D. G., Gibson, B. K., Staveley-Smith, L., Freeman, K. C., & Kilborn, V. A. 2007, *ApJ*, 662, 959
- Preston, G. W., Schectman, S. A., & Beers, T. C. 1991, *ApJS*, 76, 1001
- Putman, M. E., Gibson, B. K., Staveley-Smith, L., et al. 1998, *Nature*, 394, 752
- Putman, M. E., Bland-Hawthorn, J., Veilleux, S., Gibson, B. K., Freeman, K. C., & Maloney, P. R. 2003, *ApJ*, 597, 948
- Putman, M. E., Peek, J. E. G., Muratov, A., Gnedin, O. Y., Hsu, W., Douglas, K. A., Heiles, C., Stanimirovic, S., Korpela, E. J., & Gibson, S. J. 2009, *ApJ*, 703, 1486
- Rand, R. J. 2000, *ApJ*, 537, L13
- Rand, R. J., & van der Hulst, J. M. 1993a, *AJ*, 105, 2098
- Rand, R. J., & van der Hulst, J. M. 1993b, *AJ*, 107, 392
- Reach, W. T., Koo, B.-C., & Heiles, C. 1994, *ApJ*, 429, 672
- Richter, P., Savage, B. D., Wakker, B. P., Sembach, K. R., & Kalberla, P. M. W. 2001a, *ApJ*, 549, 281
- Richter, P., Sembach, K. R., Wakker, B. P., Savage, B. D., Tripp, T. M., Murphy, E. M., Kalberla, P. M. W., & Jenkins, E. B. 2001b, *ApJ*, 559, 318
- Richter, P., Sembach, K. R., Wakker, B. P., & Savage, B. D. 2001c, *ApJ*, 562, L181
- Richter, P., Wakker, B. P., Savage, B. D., & Sembach, K. R. 2003, *ApJ*, 586, 230
- Rosen, A., & Bregman, J. N. 1995, *ApJ*, 440, 634
- Ryans, R. S. I., Keenan, F. P., Sembach, K. R., & Davies, R. D. 1997, *MNRAS*, 289, 83
- Sancisi, R., & Allen, R. J. 1979, *A&A*, 74, 73
- Sancisi, R., Fraternali, F., Oosterloo, T. A., & van der Hulst, J. M. 2008, *A&ARv*, 15, 189

- Savage, B. D., & Sembach, K. R. 1996, *ARA&A*, 34, 279
- Savage, B. D., & Wakker, B. P. 2009, *ApJ*, 702, 1472
- Savage, B. D., Meade, M. R., & Sembach, K. R. 2001, *ApJS*, 136, 631
- Savage, B. D., Sembach, K. R., Wakker, B. P., Richter, P., Meade, M., Jenkins, E. B., Shull, J. M., Moos, H. W., & Sonneborn, G. 2003, *ApJS*, 146, 125
- Schaap, W. E., Sancisi, R., & Swaters, R. A. 2000, *A&A*, 356, L49
- Schlüter, A., Schmidt, H., & Stumpff, P. 1953, *Zeitschrift für Astrophysik*, 33, 194
- Schwarz, U. J., & Oort, J. H. 1981, *A&A*, 101, 305
- Schwarz, U. J., & Wakker, B. P. 2004, in *High-Velocity Clouds, Astrophysics and Space Science Library*, Vol. 312 (Dordrecht: Kluwer), 145
- Schwarz, U. J., Wakker, B. P., & van Woerden, H. 1995, *A&A*, 302, 364
- Sembach, K. R., & Savage, B. D. 1992, *ApJS*, 83, 147
- Sembach, K. R., Savage, B. D., & Massa, D. 1991, *ApJ*, 372, 81
- Sembach, K., Savage, B. D., Lu, L., & Murphy, E. M. 1995, *ApJ*, 451, 616
- Sembach, K., Savage, B. D., Lu, L., & Murphy, E. M. 1999, *ApJ*, 515, 108
- Sembach, K. R., Howk, J. C., Savage, B. D., & Shull, J. M. 2001, *AJ*, 121, 992
- Sembach, K. R., Gibson, B. K., Fenner, Y., & Putman, M. E. 2002, *ApJ*, 572, 178
- Sembach, K. R., Wakker, B. P., Savage, B. D., Richter, P., Meade, M., Shull, J. M., Jenkins, E. B., Sonneborn, G., & Moos, H. W. 2003, *ApJS*, 146, 165
- Sembach, K. R., Wakker, B. P., Tripp, T. M., Richter, P., Kruk, J. W., Blair, W. P., Moos, H. W., Savage, B. D., Shull, J. M., York, D. G., Sonneborn, G., Hébrard, G., Ferlet, R., Vidal-Madjar, A., Friedman, S. D., & Jenkins, E. B. 2004, *ApJS*, 150, 387
- Shapiro, P. R., & Benjamin, R. 1991, *PASP*, 103, 923
- Shapiro, P. R., & Field, G. B. 1976, *ApJ*, 205, 762
- Shelton, R. 1998, *ApJ*, 504, 785
- Shelton, R. L., Sallmen, S. M., & Jenkins, E. B. 2007, *ApJ*, 659, 365
- Shull, J. M., Stevans, M., Danforth, C., Penton, S. V., Lockman, F. J., & Arav, N. 2011, *ApJ*, 739, 105
- Sirko, E., Goodman, J., Knapp, G. R., Brinkmann, J., Ivezić, Ž., Knerr, E. J., Schlegel, D., Schneider, D. P., & York, D. G. 2004, *AJ*, 127, 899
- Slavin, J. D., Shull, J. M., & Begelman, M. C. 1993, *ApJ*, 407, 83
- Smoker, J. V., Hunter, I., Kalberla, P. M. W., Keenan, F. P., Morras, R., Hanuschik, R., Thompson, H. M. A., Silva, D., Bajaja, E., Pöppel, W. G. L., & Arnal, M. 2007, *MNRAS*, 378, 947
- Snowden, S. L., Egger, R., Finkbeiner, D. P., Freyberg, M. J., & Plucinsky, P. P. 1998, *ApJ*, 493, 715
- Spitzer, L. 1956, *ApJ*, 124, 20
- Spitzer, L. 1998, *Physical Processes in the Interstellar Medium* (New York: Wiley-VCH)
- Stocke, J. T., Penton, S. V., Danforth, C. W., Shull, J. M., Tumlinson, J., & McClintock, K. M. 2006, *ApJ*, 641, 217
- Stoppelenburg, P. S., Schwarz, U. J., & van Woerden, H. 1998, *A&A*, 338, 200
- Sutherland, R. S., & Dopita, M. A. 1993, *ApJS*, 88, 253
- Swaters, R. A., Sancisi, R., & van der Hulst, J. M. 1997, *ApJ*, 491, 140
- Thilker, D. A., Braun, R., & Walterbos, R. A. M. 1998, *A&A*, 332, 429
- Thilker, D. A., Braun, R., Walterbos, R. A. M., Corbelli, E., Lockman, F. J., Murphy, E., & Madalena, R. 2004, *ApJ*, 601, L39
- Thom, C., Putman, M. E., Gibson, B. K., Christlieb, N., Flynn, C., Beers, T. C., Wilhelm, R., & Lee, Y. S. 2006, *ApJ*, 637, L97
- Thom, C., Peek, J. E. G., Putman, M. E., Heiles, C., Peek, K. M. G., & Wilhelm, R. 2008, *ApJ*, 684, 364
- Tripp, T. M., Wakker, B. P., Jenkins, E. B., Bowers, C. W., Danks, A. C., Green, R. F., Heap, S. R., Joseph, C. L., Kaiser, M. E., Linsky, J. L., & Woodgate, B. E. 2003, *AJ*, 125, 3122
- Tufte, S. L., Reynolds, R. J., & Haffner, L. M. 1998, *ApJ*, 504, 773
- van Dishoeck, E. F., & Black, J. H. 1986, *ApJS*, 62, 109
- van der Hulst, J. M., & Sancisi, R. 1988, *AJ*, 95, 1354
- van der Hulst, J. M., van Albada, T. S., & Sancisi, R. 2001, in *Gas and Galaxy Evolution*, ASPC 240 (San Francisco, CA: Astronomical Society of the Pacific), 451
- van Woerden, H., & Wakker, B. P. 2004, in *High-Velocity Clouds, Astrophysics and Space Science Library*, Vol. 312 (Dordrecht: Kluwer), 195
- van Woerden, H., Schwarz, U. J., Peletier, R. F., Wakker, B. P., & Kalberla, P. M. W. 1999a, *Nature*, 400, 138
- van Woerden, H., Peletier, R. D., Schwarz, U. J., Wakker, B. P., & Kalberla, P. M. W. 1999b, in *ASP Conf. Ser. 166, Stromlo Workshop on High-Velocity Clouds*, eds. B. K. Gibson, & M. E. Putman (San Francisco, CA: ASP), 1
- van Woerden, H., Wakker, B. P., Schwarz, U. J., & de Boer, K. S., eds. 2004, *High-Velocity Clouds, Astrophysics and Space Science Library*, Vol. 312 (Dordrecht: Kluwer)
- Verheijen, M. A. W., & Sancisi, R. 2001, *A&A*, 370, 765

- Wakker, B. P. 1991, *A&A*, 250, 499
- Wakker, B. P. 2001, *ApJS*, 136, 463
- Wakker, B. P. 2004, in *High-Velocity Clouds, Astrophysics and Space Science Library*, Vol. 312 (Dordrecht: Kluwer), 25
- Wakker, B. P. 2006, *ApJS*, 163, 282
- Wakker, B. P., & Boulanger, F. 1986, *A&A*, 170, 84
- Wakker, B. P., & Mathis, J. S. 2000, *ApJ*, 544, L107
- Wakker, B. P., & Savage, B. D. 2009, *ApJS*, 182, 378
- Wakker, B. P., & Schwarz, U. J. 1991, *A&A*, 250, 484
- Wakker, B. P., & van Woerden, H. 1991, *A&A*, 250, 509
- Wakker, B. P., & van Woerden, H. 1997, *ARA&A*, 35, 217
- Wakker, B. P., Howk, C., Schwarz, U. J., van Woerden, H., Beers, T., Wilhelm, R., Kalberla, P., & Danly, L. 1996, *ApJ*, 473, 834
- Wakker, B. P., Murphy, E.M., van Woerden, H., & Dame, T. M. 1997, *ApJ*, 488, 216
- Wakker, B. P., van Woerden, H., de Boer, K. S., & Kalberla, P. M. W. 1998, *ApJ*, 493, 762
- Wakker, B. P., Howk, J. C., Savage, B. D., van Woerden, H., Tufté, S. L., Schwarz, U. J., Benjamin, R., Reynolds, R. J., Peletier, R. F., & Kalberla, P. M. W. 1999, *Nature*, 402, 388
- Wakker, B. P., Kalberla, P. M. W., van Woerden, H., de Boer, K. S., & Putman, M. E. 2001, *ApJS*, 136, 537
- Wakker, B. P., Oosterloo, T. A., & Putman, M. E. 2002, *AJ*, 123, 1953
- Wakker, B. P., York, D. G., Howk, J. C., Barentine, J. C., Wilhelm, R., Peletier, R. F., van Woerden, H., Beers, T. C., Ivezić, Z., Richter, P. R., & Schwarz, U. J. 2007, *ApJ*, 670, L113
- Wakker, B. P., York, D. G., Wilhelm, R., Barentine, J. C., Richter, P., Beers, T. C., Ivezić, Z., & Howk, J. C. 2008, *ApJ*, 672, 298
- Wakker, B. P., Lockman, F. J., & Brown, J. 2011, *ApJ*, 728, 159
- Wakker, B. P., Savage, B. D., Fox, A. J., Benjamin, R., & Shapiro, P. 2012, *ApJ*, 749, 157
- Wannier, P., Wrixon, G. T., & Wilson, R. W. 1972, *A&A*, 18, 224
- Weiner, B. J., & Williams, T. B. 1996, *AJ*, 111, 1156
- Weiss, A., Heithausen, A., Herbstmeier, U., & Mebold, U. 1999, *A&A*, 344, 955
- Westmeier, T., Braun, R., & Thilker, D. A. 2005, *A&A*, 436, 101
- Westmeier, T., Brüns, C., & Kerp, J. 2008, *MNRAS*, 390, 1691
- White, S. D. M., & Rees, M. J. 1978, *MNRAS*, 183, 341
- Winkel, B., Kalberla, P. M. W., Kerp, J., & Flöer, L. 2010, *ApJS*, 188, 488
- York, D. G., et al. 2000, *AJ*, 120, 1579
- Zwaan, M. A. 2001, *MNRAS*, 325, 1142